A Constitutive Heterochromatic Region Shapes Genome Organization and Impacts Gene Expression in *Neurospora crassa*

Andrew T. Reckard[1], Abhishek Pandeya[2]*, Jacob M. Voris[1]*, Carlos G. Gonzalez Cruz[1], Oluwatosin Oluwadare[2], and Andrew D. Klocko[1‡]

[1]Department of Chemistry & Biochemistry, University of Colorado Colorado Springs, Colorado Springs, CO 80918, USA

[2]Department of Computer Science, University of Colorado Colorado Springs, Colorado Springs, CO 80918, USA

*Equal Contribution

[‡]Corresponding Author: Andrew D. Klocko, email: aklocko@uccs.edu

Author Contributions: A.T.R. and A.D.K. designed research; A.T.R., A.P., J.V., C.G.C, O.O. and A.D.K. performed research; A.T.R., A.P., J.V., C.G.C., O.O. and A.D.K. analyzed data; and A.T.R., A.P., J.V., C.G.C., O.O. and A.D.K. wrote the paper.

Abstract

Genome organization is essential for proper function, including gene expression. In metazoan genome organization, chromatin loops and Topologically Associated Domains (TADs) facilitate local gene clustering, while chromosomes form distinct nuclear territories characterized by compartmentalization of silent heterochromatin at the nuclear periphery and active euchromatin in the nucleus center. A similar hierarchical organization occurs in the fungus *Neurospora crassa* where its seven chromosomes form a Rabl conformation, where heterochromatic centromeres and telomeres independently cluster at the nuclear membrane, while interspersed heterochromatic loci in Neurospora aggregate across megabases of linear genomic distance for forming TAD-like structures. However, the role of individual heterochromatic loci in normal genome organization and function is unknown. Here, we examined the genome organization of a Neurospora strain harboring a ~47.4 kilobase facultative (temporarily silent) heterochromatic region deletion, as well as the genome organization of a strain deleted of a 110.6 kilobase permanently silent constitutive heterochromatic region. While the facultative heterochromatin deletion had little effect on local chromatin structure, the constitutive heterochromatin deletion altered local TAD-like structures, gene expression, and the predicted 3D genome structure by qualitatively repositioning genes into the nucleus center. Our work elucidates the role of individual heterochromatic regions for genome organization and function.

Keywords: genome organization, chromosome conformation, heterochromatin, *Neurospora crassa*, gene expression

46 **Introduction**

47 The correct organization of a genome, including proper chromosome folding, is necessary for
48 the function of DNA-templated processes, including gene expression regulation (1–5). Indeed,
49 improper DNA folding altering transcriptional patterns occurs in human cancer cells (6–8).
50 Eukaryotic genomes are hierarchically folded in nuclei, where DNA molecules are wrapped about
51 histone octamers to form chromatin fibers that are extruded into globules ("loops") by cohesin and
52 compacted into Topologically Associated Domains (TADs) (9–17). TADs of similar transcriptional
53 activity are then compartmentalized into the nucleus (10, 11, 17). Specifically, the more open,
54 gene-rich, and actively transcribed euchromatin primarily localizes to the nucleus center, while the
55 silent, often gene-poor, and compacted heterochromatin is confined to the nuclear periphery (18–
56 20). Heterochromatin segregation may drive chromatin compartmentalization, although
57 transcriptional activity might force silent genomic loci to the nuclear periphery (19). In metazoans,
58 the formation of individual chromosome territories typified by reduced inter-chromosomal
59 contacts leads to the clustering of intra-chromosomal heterochromatic regions (21, 22). In contrast,
60 the independent aggregation of the heterochromatic centromeres and telomeres into the Rabl
61 conformation promotes extensive intra- and inter-chromosomal heterochromatic contacts across
62 fungal chromosomes (9, 23–25). All told, heterochromatin bundling is a conserved feature of
63 eukaryote genome organization.

64 Fungi are excellent models for studying genome organization. Resembling metazoans, fungal
65 genomes are partitioned into euchromatin and heterochromatin, and the heterochromatin of many
66 filamentous fungi, including *Neurospora crassa*, is subdivided into permanently silent constitutive
67 heterochromatin and temporarily silent facultative heterochromatin (26–28). The adenine and
68 thymine (AT)-rich, gene-poor, and repetitive constitutive heterochromatic regions, comprising

69 ~16% of the Neurospora genome, are marked by the tri-methylation of lysine 9 on histone H3
70 (H3K9me3) that is catalyzed by the histone methyltransferase DIM-5 (KMT1) (27, 29–31).
71 Specific H3K9me3-marked regions found within the seven Neurospora chromosomes ("Linkage
72 Groups" [LGs]) include the regional centromeres, the 14 telomeres, and ~200 interspersed
73 heterochromatic regions (27, 31). Neurospora facultative heterochromatin is delineated by the
74 subtelomeric di- or tri-methylation of lysine 27 on histone H3 (H3K27me2/3), which is catalyzed
75 by the SET-7 (KMT6) histone methyltransferase of the Polycomb Repressive Complex 2 (PRC2)
76 (32–34). In the Neurospora three-dimensional (3D) genome organization, as assessed by in nucleus
77 chromosome conformation capture coupled with high-throughput sequencing (*in situ* Hi-C), robust
78 intra- and inter-chromosomal heterochromatic interactions are readily observed across megabases
79 of linear genomic distance with few heterochromatin-euchromatin contacts, highlighting the
80 compartmentalization of fungal chromatin (9, 23, 24). The clustering of heterochromatic regions
81 forms the anchors of TAD-like structures; similar structures are observed in other ascomycete
82 fungi, suggesting the use of heterochromatin to organize fungal genomic DNA may be conserved
83 (9, 23–25, 35). Further, subtelomeric facultative heterochromatin enriched with H3K27me2/3
84 mediates the interaction between chromosome ends and the nuclear periphery (36). Together, both
85 heterochromatin types are necessary to organize the Neurospora genome into the Rabl
86 chromosome conformation.

87 To understand the importance of individual facultative and constitutive heterochromatic
88 regions on 3D genome organization in Neurospora, we performed chromatin-specific *in situ* Hi-C
89 on a strain harboring a deletion of a ~47.4 kilobase (kb) H3K27me2/3 domain on the LG VI left
90 arm (33), as well as a strain in which we deleted a ~110 kb H3K9me3 domain on the LG II right
91 arm. While the H3K27me2/3 deletion minimally impacts genome organization, the H3K9me3

92 deletion ("ΔLGIIK9het25") reorganizes the heterochromatin bundle and alters regional TADs
93 across LG II without affecting deposition of H3K9me3 on nearby AT-rich loci. The 3D structure
94 prediction of individual ΔLGIIK9het25 strain chromosomes is qualitatively different than those of
95 its wild type (WT) counterpart, and numerous genes became upregulated in the ΔLGIIK9het25
96 strain, possibly due to altered gene positioning within the 3D genome. We conclude that a
97 constitutive heterochromatic region organizes the *Neurospora crassa* genome for proper fungal
98 genome function.
99

100 **Results**

101 ***Loss of a H3K27me2/3-enriched region minimally affects the local chromatin landscape.***

102 Since interactions between regions of similar heterochromatin type comprise many of the
103 strongest intra-chromosomal contacts in the Neurospora genome (23, 24), we examined how
104 deletions of either type, facultative or constitutive heterochromatin, could impact fungal
105 heterochromatin clustering. Starting with facultative heterochromatin, we examined a previously
106 constructed strain, N4933, originally used to assess position-dependent signals for H3K27me2/3
107 deposition in Neurospora genome (33). N4933 harbors a 47.4 kb deletion of LG VIL, from
108 basepairs 175,121 to 222,557, which removes fourteen H3K27me2/3-enriched genes ("ΔK27").
109 To assess how ΔK27 impacts genome organization, we performed two *in situ* Hi-C replicates with
110 *Dpn*II to capture gene-rich chromatin interactions within DNA of higher guanine and cytosine
111 basepair percentages, including those in facultative heterochromatic regions, in the nucleus. Our
112 replicates show highly similar Hi-C contact matrices across LG VI and are highly correlated
113 (Figure S1), allowing replicate merging into a single Hi-C dataset with 9.2 million (M) valid reads.
114 For comparison, we processed an identical number of valid Hi-C reads from our WT *in situ Dpn*II

115 Hi-C dataset (23). Our initial observation is that, despite having nearly identical valid reads, the
116 ΔK27 dataset has a slight bias in capturing more local contacts, most likely due to Hi-C experiment
117 variability, which concomitantly reduces inter-chromosomal contacts. Indeed, decreased inter-
118 centromeric contacts are observed in raw datasets due to fewer centromeric *Dpn*II sites (Figures 1,
119 S2-S3). Inter-centromeric interactions are present upon Knight-Ruiz (KR) (37) correction (Figure
120 S3), indicating capture of biologically relevant structures. Upon directly comparing WT and ΔK27
121 contact matrices, the decrease in moderate and long-range contacts is evident (Figure S3).
122 Therefore, we focused our analyses on the local LG VIL changes that manifest with the
123 H3K27me2/3 region deletion.

124 On WT LG VI, we observe consistent off-diagonal contacts that inversely decrease with
125 genomic distance, in addition to strong inter-telomeric contacts and the insulation of centromeric
126 DNA from local euchromatin, in both raw and KR corrected heatmaps (Figure 1A). A higher
127 resolution (5kb) heatmap of the 500 kb surrounding the region deleted in N4933 shows a gradual
128 decrease of contacts from the diagonal (Figure 1A). In contrast, the ΔK27 deletion Hi-C, mapped
129 to the Neurospora reference genome version 14 ("nc14") (23), appears as a white cross emanating
130 from the deletion locus indicating a gap in mappable Hi-C reads (Figure 1B), since the DNA in
131 this region was not present for nuclear ligation capture. This gap occurs in both the raw and KR
132 corrected contact probability heatmaps, although the base of the diagonal on the KR corrected
133 heatmap has some signal (Figures 1B-C), perhaps due to correctional bias. Importantly, stronger
134 off diagonal signal at the boundary intersections of the facultative heterochromatin deletion appear
135 (Figures 1B-C, black arrowheads), showing how new interactions occur between the
136 H3K27me2/3-enriched chromatin flanking the ΔK27 deletion. Interestingly, another N4933 locus
137 devoid of Hi-C signal is observed over the *sly1-1* transposase gene NCU09969 (Figure 1C, gray

138 arrowhead), suggesting the ΔK27 strain had a transposition event. Regarding telomere clustering,
139 the ΔK27 strain is still capable of forming intra- and inter-chromosomal subtelomeric interactions
140 (Figures 1D-E), with strong contacts between chromosome ends originating from the terminal
141 ~100kb chromatin enriched with H3K27me2/3. We conclude a deletion of a H3K27me2/3-
142 enriched region minimally impacts the organization of the remaining LGVIL facultative
143 heterochromatin.
144
145 ***Deletion of a ~110 kb constitutive heterochromatic region alters silent region clustering.***
146 In Neurospora nuclei, gene-poor AT-rich constitutive heterochromatin is compartmentalized
147 from gene-rich euchromatin or facultative heterochromatin (23, 38). To ask if altered constitutive
148 heterochromatin composition could have consequences on genome organization and function, we
149 deleted a 110,609 bp H3K9me3-enriched region on LG IIR, aptly called "LGIIK9het25" as this
150 region is the 25th constitutive heterochromatic region from the LG II left telomere. We chose
151 LGIIK9het25 for deletion for a high probability of observing changes to genome organization by
152 deleting a large AT-rich region without compromising chromosome function by removing the
153 centromere. Using split-marker homologous recombination in a D*mus-52* strain (39), we replaced
154 the 110.6 kb LGIIK9het25 with a hygromycin resistance gene (hygromycin phosphotransferase;
155 *hph*) controlled by a strong constitutive *trpC* promoter (a P_{trpC}*::hph* construct; Figure S4A). We
156 note a similar-sized DNA replacement could have more accurately represented the LG II
157 chromosome length, but we wanted to avoid cryptic promoters, repetitive sequences for RIP (27,
158 40, 41), or AT-rich DNA sequences forming novel constitutive heterochromatic regions within the
159 inserted DNA. We successfully obtained hygromycin-resistant primary transformants containing
160 the LGIIK9het25 deletion (DLGIIK9het25); in sum, we removed 109,208 bp from the Neurospora

161 genome, given that P_{trpC}*::hph* inserts 1,401 bp. A hygromycin-resistant progeny from a sexual
162 cross, xKL9AR-17, was characterized by PCR analysis as harboring both the DLGIIK9het25 allele
163 (Figure S4B) and a wild type *mus-52*$^{+}$ allele. The final strain, NKL2 (genotype: *mat A*;
164 D*LGIIK9het25::hph*), had no noticeable growth defect from a WT strain (Figure S4C-D).

165 We performed chromatin-specific Hi-C (23) using the restriction enzyme *Dpn*II to monitor the
166 contacts of gene-rich euchromatin, while *Mse*I Hi-C captures interactions between AT-rich, gene-
167 poor constitutive heterochromatic regions. Our *Dpn*II and *Mse*I DLGIIK9het25 Hi-C replicates
168 show highly reproducible and correlated interactions (Figure S5), allowing us to merge replicates
169 into enzyme-specific datasets, with the NKL2 *Dpn*II dataset containing 20.6M valid reads and the
170 NKL2 *Mse*I dataset comprising 12.2M valid reads. All Hi-C datasets display the inter-
171 chromosomal centromeric interactions independent of telomere clusters, indicating our Hi-C
172 captured biologically relevant structures (Figures S6-S7). As before, we selected nearly identical
173 valid read numbers from previously published WT *Dpn*II and *Mse*I datasets for comparisons (23).

174 Compared to a WT *Dpn*II Hi-C dataset (Figure 2A), the deleted LGIIK9het25 region appears
175 as a large white "cross" devoid of Hi-C interactions on LGII in the NKL2 *Dpn*II contact probability
176 matrix (Figure 2B). Looking specifically at a 500 kb region surrounding LGIIK9het25, the WT
177 dataset has extensive interactions within and around LGIIK9het25, while the NKL2 has contact
178 probability loss, as no interactions are observed in the raw interaction heatmap and sparse contacts
179 at the diagonal in the KR corrected dataset (Figure 2A-B), which may be due to a few reads
180 mapping to repetitive DNA sequences at this locus. The Hi-C contacts surrounding DLGIIK9het25
181 appear slightly enhanced, as the flanking euchromatin moderately gains contacts in the NKL2
182 *Dpn*II dataset, relative to a WT dataset (Figure 2A-B). Similar contact probability changes occur
183 in WT and NKL2 *Mse*I datasets, where in the WT dataset the LGIIK9het25 region extensively

184 contacts internal heterochromatin yet is isolated from surrounding euchromatin, but the NKL2
185 dataset completely loses heterochromatic contacts from the LGIIK9het25 region yet gains flanking
186 euchromatin interactions (Figure 2C-D). Direct comparison of the WT and NKL2 *Dpn*II and *Mse*I
187 datasets surrounding LGIIK9het25 shows the contact probability gain between flanking
188 euchromatic regions when a separating heterochromatic region is lost (Figure 2E-F, arrowheads).
189 This surrounding euchromatin may gain local, on-diagonal interactions, as shown in the *Mse*I
190 comparison (Figure 2F), possibly due to either reduced heterochromatic interactions or a local
191 contact capture bias in the NKL2 dataset. Between LG I and LG II, the LGIIK9het25 deletion
192 causes a loss of inter-heterochromatic region interactions, including from the largest non-
193 centromeric heterochromatic region on LG I (Figure 2G, white arrowhead), while the LG II
194 centromere loses inter-centromeric contacts but modestly gains interactions with interspersed
195 heterochromatic regions (Figure 2G, black arrowhead). Similar gains in inter-heterochromatic
196 region interactions are evident across the genome in WT vs. NKL2 *Mse*I Hi-C dataset comparisons
197 (Figure S8), possibly from the absence of LGIIK9het25 contacts influencing euchromatin
198 interactions. As evident in WT vs. NKL2 *Dpn*II comparisons, the inter-chromosomal contact
199 strength between centromere-proximal euchromatin and more-distant euchromatin on
200 chromosome arms is increased, yet chromosome-internal euchromatic contacts are reduced (Figure
201 S9), possibly due to enhanced centromere-interspersed heterochromatin bundling. Similarly, both
202 DLGIIK9het25 Hi-C datasets have depleted inter-centromeric contacts; KR correction reduces
203 *Dpn*II contact biases (Figures S8-S9). All told, the LGIIK9het25 deletion moderately impacts the
204 organization of the entire Neurospora genome.
205
206 ***The LGIIK9het25 deletion minimally alters H3K9me3 deposition but alters TAD-like structures.***

207 Upon deleting LGIIK9het25, the possibility exists that genome function, specifically
208 H3K9me3 deposition on nearby AT-rich loci, may be impacted. To assess if constitutive
209 heterochromatic region loss limits histone post-translational modification enrichment, we
210 performed H3K9me3 Chromatin Immunoprecipitation-sequencing (ChIP-seq) on the NKL2
211 strain. Our two H3K9me3 ChIP-seq replicates were highly reproducible (Figure S10) and were
212 merged into a single Reads Per Kilobase per Million (RPKM) normalized file for direct
213 comparison to previously published WT H3K9me3 ChIP-seq datasets, although using spike-in
214 DNA controls may be best practice for assessing strain differences (42, 43). We mapped the ChIP-
215 seq reads to either the nc14 WT genome or an "NKL2 reference genome" which replaced the AT-
216 rich DNA of LGIIK9het25 with the P_{trpC}*::hph* sequence; enhanced images show low levels of
217 background signal across the P_{trpC}*::hph* sequence in an NKL2 H3K9me3 ChIP-seq dataset that are
218 absent in WT H3K9me3 data (Figure S4E).

219 H3K9me3 ChIP-seq enrichment exhibits similar patterns across LG II, independent of the
220 reference genome used for mapping reads. For ChIP-seq data mapped to the WT nc14 genome,
221 identical H3K9me3-enriched regions are observed, except peaks to the right of LGIIK9het25 are
222 shifted by ~110kb from the deletion site (Figure 3A), given that genomic elements positions within
223 bedgraph/bigwig enrichment count files are shifted based on input bam file read mapping position.
224 Qualitatively, the NKL2 H3K9me3 peaks are higher (Figure 3A), possibly reflecting increased
225 H3K9me3 purification from the remaining constitutive heterochromatic regions or enhanced
226 sequencing depth limiting background signal. When H3K9me3 ChIP-seq data from both strains
227 was mapped to the NKL2 reference genome, the loss of LGIIK9het25 signal from the WT dataset
228 is apparent, while the remaining constitutive heterochromatic regions have identical LG II genomic
229 positions (Figure 3B).

230 To further assess local chromatin changes with the LGIIK9het25 deletion, we examined
231 Topologically Associated Domain (TAD)-like structure positions on LG IIR. The TAD-like
232 structures in WT and NKL2 *Dpn*II datasets, mapped to the nc14 (WT) genome, show striking
233 differences across euchromatin, with larger TAD-like structures predicted with the ΔLGIIK9het25
234 allele, as opposed to the smaller TAD-like structures in WT datasets (Figure 4A), although TAD
235 structure prediction can vary (44). To more clearly understand the strain-specific chromatin folding
236 changes without the ΔLGIIK9het25 signal gap, we predicted TAD-like structures WT and NKL2
237 *Dpn*II and *Mse*I datasets mapped to the NKL2 reference genome. Here, clear changes to TAD-like
238 structures are observed at the deletion site, with the euchromatin in the *Dpn*II dataset having larger
239 TAD-like structures in the NKL2 strain, while the NKL2 ΔLGIIK9het25 *Mse*I strain has smaller
240 TAD-like structures on the diagonal (Figure 4B, black arrowheads), with this difference likely
241 stemming from the chromatin monitored – and the density of restriction sites – in each Hi-C
242 experiment. The flanking TAD-like structures are nearly identical in both datasets, except for two
243 larger TADs-like structures in the NKL2 *Mse*I data (Figure 4B, open arrowheads). Interestingly, at
244 the P_{trpC}*::hph* insertion, two novel yet small TAD-like structures are observed in both NKL2
245 datasets, combined with additional stronger Hi-C interactions in *Mse*I data (Figure 4B, purple line),
246 suggesting the constitutive P_{trpC} promoter could influence local contacts – and possibly regulate
247 expression – of nearby genes. Overall, the deletion of the constitutive heterochromatic region
248 LGIIK9het25 alters the local folding of the euchromatin surrounding the deletion site.
249

250 ***The LGIIK9het25 deletion alters the three-dimensional folding of Neurospora chromosomes.***

251 It remained possible that a large constitutive heterochromatic region deletion would alter
252 chromosome folding. To assess the 3D folding of LG II, we computationally predicted the LG II

253 3D structure using WT and NKL2 ΔLGIIK9het25 Hi-C datasets. We chose to merge all *Dpn*II and
254 *Mse*I data together from each strain to maximize the possible Hi-C contacts across their genomes;
255 we did not combine *Dpn*II and *Mse*I data at ratios equivalent to the Neurospora chromatin
256 distribution, as previously performed (23). With the maximal contact probability merged matrices,
257 we iteratively generated LG II 3D structures using 3DMax (45) customized for biologically
258 relevant structures in fungal genomes.

259 In the WT strain, LG II has an elongated structure with condensed chromosome arms, a more
260 isolated centromere, telomeres localized to a single "side", and extensive intervening chromatin
261 loops (Figure 5A). Similar 3D structure prediction changes are observed on the other six WT
262 chromosomes (Figure S11). The LGIIK9het25 region forms a loop and associates with nearby
263 chromatin loops (Figure 5A), consistent with the presence of nine, moderately sized
264 heterochromatic regions in the terminal 800 kb of the LG II right arm (Figure 3A). In contrast, the
265 chromosome arms within the LG II 3D structure when LGIIK9het25 is deleted are more compact
266 and form a wider structure, despite similar centromere isolation, telomere locations, and looping
267 of intervening chromatin (Figure 5B). In fact, the terminal right arm of NKL2 LG II does not form
268 any loops in this 3D structure prediction, suggesting that the requirement for telomere clustering
269 impacts the chromosome folding prediction in the NKL2 strain (Figure 5B). Similar folding
270 differences occur on each LG in NKL2, with some chromosomes - specifically LG I and LG IV -
271 having drastically altered 3D structures relative to WT LG folding (Figures S11, S12). Together,
272 the deletion of a ~110kb constitutive heterochromatic region modifies the predicted 3D structures
273 of Neurospora LGs.

274

275 ***The LGIIK9het25 deletion increases gene expression due to altered 3D genome folding.***

To understand if constitutive heterochromatin could influence genome function through gene expression, we assessed changes in polyadenylation messenger RNA sequencing (polyA mRNA-seq) in WT and NKL2 ΔLGIIK9het25 strains. As a control for complete loss of constitutive heterochromatin function, we examined gene expression changes in a Δ*dim-5* strain, which is devoid of H3K9me3 genome-wide (29). Volcano plots that display the significant gene expression changes ($\log_2 > 3.0$ or < -3.0; adjusted p-value < 0.001) in the NKL2 strain relative to the WT strain show 84 genes are significantly upregulated and no genes significantly downregulated, (Figure 6A, left; Supplementary File S1), consistent with the removal of a repressive heterochromatic region; additional genes could be considered differentially regulated with less stringent cutoff values. In contrast, the Δ*dim-5* strain has 175 differentially regulated genes compared to WT, with genes having both increased and decreased transcription (Figure 6A, right; Supplementary File S2), including the strong reduction of the gene NCU04402 encoding DIM-5 (Figure 6B), highlighting our polyA mRNA-seq dataset accuracy. Many Δ*dim-5* differentially expressed genes associate with altered peaks of H3K27me2/3 (Figure S13), as this facultative heterochromatin mark relocates to constitutive heterochromatic regions in a Δ*dim-5* strain (46, 47). Unique genes are found in the ΔLGIIK9het25 and Δ*dim-5* datasets, with only 25 overlapping differentially regulated genes. Notably, ΔLGIIK9het25 causes less drastic expression changes relative to the Δ*dim-5* polyA mRNA-seq (Figure 6A-B). Further, there are no differentially expressed genes in the ΔLGIIK9het25 strain wtih putative functions in chromatin or transcriptional regulation (Supplementary File S3), although numerous hypothetical genes without defined functions are present, preventing a complete assessment of possible genes involved in regulating transcription. Interestingly, gene expression changes in the ΔLGIIK9het25 strain occur on each chromosome (Figures 6B, S14), with many genes near H3K9me3-marked heterochromatic

299 regions. Specifically, the gene NCU08696, directly adjacent to LGIIK9het25, is downregulated in
300 the Δ*dim-5* strain but upregulated in ΔLGIIK9het25 (Figure 6B, zoomed region), the latter possibly
301 due to its proximity to the strong P_{trpC} promoter. While longer chromosomes would be expected to
302 have more differentially expressed genes, the short ~4.3 Mb LG VII has more genes with changed
303 expression (n = 24 differentially expressed genes [DEGs]) than either the ~10 Mb LG I (n = 20
304 DEGs) or the 6.0 Mb LG IV (n =11 DEGs) (Figures 6B and S14, Supplementary File S2). We
305 conclude that a constitutive heterochromatic region controls gene expression across the fungal
306 genome.

307 To assess if altered 3D chromosome folding could explain the transcriptional changes in a
308 ΔLGIIK9het25 strain, we colored bins harboring differentially expressed genes on models of
309 NKL2 LGs. Qualitatively, the positions of the bins containing the differentially expressed genes
310 are modified on the 3D chromosome structures in the ΔLGIIK9het25 strain relative to the WT
311 strain (Figures 6C-D, S15, S16). Specifically, on LG II, the bins with differentially expressed genes
312 appear more "enclosed" within the WT structure, while these same bins are repositioned to another
313 "face" of the NKL2 LG II structure (Figure 6C-D). Similar qualitative bin movements altering
314 gene positions are readily observed on other LGs (Figure S16).

315 Finally, we examined the positions of ΔLGIIK9het25 differentially expressed genes relative to
316 the 3D folding predicted for the WT and NKL2 genomes. Our 3D genome models maintain the
317 biologically relevant centromere cluster independent of the bundling of telomeres (Figure S17).
318 The WT genome model forms an elongated structure with the LGIIK9het25 region close to the
319 structure bottom (Figure 7A), consistent with the "stretched" conformation of individual
320 chromosomes (Figures 5, S15-S16) and a previous report (48), despite different programs
321 predicting each 3D structure. The NKL2 genome deleted of LGIIK9het25 is wider and less

322 elongated (Figure 7B), similar to the individual NKL2 chromosomes. Intriguingly, the 20 kb bins
323 containing the ΔLGIIK9het25 differentially expressed genes are qualitatively oriented towards the
324 WT genome periphery, while the same bins are more centrally localized in the NKL2 genome,
325 consistent with the increased gene expression that occurs with the LGIIK9het25 deletion. We
326 conclude that the loss of a single heterochromatic region alters the 3D conformation of the genome
327 and disrupts normal genome function in the Neurospora nucleus.
328

329 **Discussion**

330 Here, we examined if facultative and constitutive heterochromatic regions organize the fungal
331 genome by performing Hi-C on strains harboring silent region deletions. Our results suggest that
332 gene-rich facultative heterochromatic loci are plastic in nature, as a facultative heterochromatin
333 deletion simply fuses nearby H3K27me2/3-enriched regions within the linear chromosome, which
334 minimally impacts facultative heterochromatin clustering. Specifically, the subtelomere bundling
335 at the terminal ~150 kb of each LG is maintained in the facultative heterochromatin deletion strain.
336 Subtelomere clustering may be compromised by larger deletions or only deletions targeting the
337 terminal ~150 kb of a chromosome. Consistent with these hypotheses, genome-wide loss of
338 H3K27me2/3 in a Neurospora Δ*set-7* (Δ*kmt-6*) strain causes subtelomere cluster dissociation from
339 the nuclear periphery (36), suggesting at least some subtelomeric H3K27me2/3 is needed for
340 nuclear membrane association. While larger or telomere-proximal deletions of facultative
341 heterochromatin could assess subtelomere clustering requirements, Neurospora may endure
342 alterations to gene-rich genomic loci, assuming no essential genes are deleted, given the absence
343 of wide-ranging topological or physiological consequences. Since most genes enriched with
344 H3K27me2/3 are novel genes with a hypothetical function (32), Neurospora may tolerate

345 subtelomeric structural variants if facultative heterochromatin is deposited. In contrast, some
346 Fusarium species require H3K27me2/3 for normal growth (49), meaning facultative
347 heterochromatic structural variants may be selected against in Fusarium.

348 We also assessed the role of a constitutive heterochromatic region for organizing the
349 Neurospora genome. The most recent Neurospora reference genome (nc14) (23) has ~200
350 interspersed H3K9me3-enriched regions distributed across its seven chromosomes, and apart from
351 the regional centromeres and telomeres of each LG required for chromosome function, the
352 remaining interspersed heterochromatic regions have often been dismissed as "junk DNA".
353 However, when we delete the largest, non-centromeric heterochromatic region on LG II, genome
354 organization and function are impacted. Specifically, the remaining heterochromatic regions have
355 altered clustering when LGIIK9het25 is deleted, as increases in intra- and inter-chromosomal
356 heterochromatic region contacts are observed, including between interspersed heterochromatic
357 regions and centromeres. These data suggest the Neurospora heterochromatin bundle is dynamic,
358 with no "defined" interactions mediated by specific DNA binding motifs in each heterochromatic
359 region. Thus, heterochromatic region aggregation mediated by Liquid Liquid Phase Separation or
360 a chromatin binding protein, such as Heterochromatin Protein-1 (HP1) (50–52) may allow shifting
361 contacts between constitutive heterochromatic regions. Since HP1 loss does not radically disrupt
362 the Neurospora heterochromatin bundle (24), perhaps a combination of redundant factors drive
363 silent chromatin bundling in fungi. Similarly, HP1-independent pericentromere clustering is
364 observed in Drosophila (53). Future experiments may elucidate additional mechanisms necessary
365 for heterochromatin clustering in eukaryotes.

366 The LGIIK9het25 deletion also showed changes in the local chromatin structure and the
367 folding of the 3D genome. In a manner synonymous to the deletion of the H3K27me2/3 region,

368 the loss of LGIIK9het25 caused the flanking chromatin to simply "fuse", as shown by interaction
369 gains between neighboring euchromatin bins. However, removing the intervening permanently
370 silent region causes the predicted TADs within this newly fused chromatin to change – forming a
371 larger TAD-like structure comprised of unique chromatin loops, suggesting the loss of
372 LGIIK9het25 alters the regional chromatin looping. Since interspersed heterochromatic regions in
373 Neurospora and other filamentous fungi act as "anchors" at the bases of TAD-like structures (9,
374 23–25, 35), in a mechanism tantamount to CTCF forming metazoan loops (10), removing a
375 heterochromatic "boundary element" would allow distant euchromatic regions to interact within a
376 single TAD-like structure. Complicating matters is how fungal TAD-like structures have extensive
377 inter-TAD interactions (23–25), meaning that the non-uniform TAD-like structures in Neurospora
378 may minimize the functional consequences of altering loop structures. Further, it would be
379 expected that TAD-like structures would differentially form on fungal chromosomes with different
380 patterns of interspersed heterochromatic regions. While fungi and metazoans employ different
381 chromatin folding mechanisms, it is possible that a deletion of a metazoan constitutive
382 heterochromatic region would also disrupt TADs by changing the highly isolated TAD-internal
383 interactions, in a similar manner to our observations in fungi. Here, loss of a H3K9me3-enriched
384 region from a metazoan genome could alter TAD compartmentalization or misregulate gene
385 expression if several smaller TADs are merged into a larger TAD. Unfortunately, the consequences
386 to metazoan genome function would be more dire, given how TAD boundary dysfunction
387 compromises proper gene expression (6–8). In fact, our chromosome and genome structure
388 predictions suggest local TAD changes could manifest into a completely unique folding pattern for
389 the overall genome. Here, the ΔLGIIK9het25 deletion caused each chromosome, and the entire
390 genome, to form a conformation qualitatively distinct from a wild type genome structure. While

391 these models are merely predictions and should be interpreted lightly, it is impactful that the
392 repositioning of a single locus has the potential to alter the 3D folding of the whole genome. Thus,
393 despite the species-specific differences in TADs or loops, it is hypothetically possible that syntenic
394 changes of linear chromosomal DNA could alter a species' genome organization and function.

395 Importantly, we show a novel function for a constitutive heterochromatic region, as the
396 ΔLGIIK9het25 strain is important for downregulating gene expression in a WT straiin, consistent
397 with the repressive nature of H3K9me3. The gene expression changes we observe when a single
398 constitutive heterochromatic region is deleted are not at the same extent as if all H3K9me3 is
399 removed in a Δ*dim-5* strain, with numerous genes both strongly up- and down-regulated (36),
400 suggesting the LGIIK9het25 deletion may minorly affect genome function. Overall, this single
401 constitutive heterochromatic region may subtly repress gene expression in the Neurospora
402 genome, which was hypothesized when strong gene – constitutive heterochromatin contacts were
403 observed in a high-resolution Neurospora Hi-C dataset (23). However, it is difficult to imagine that
404 the single LGIIK9het25 region deletion directly causes these gene expression changes genome
405 wide. More likely, the ΔLGIIK9het25 allele alters the positioning of the heterochromatin bundle –
406 and the nearby euchromatin – at the nuclear periphery, which repositions some gene promoters for
407 increased transcription machinery accessibility. This hypothesis is supported by modeling the gene
408 expression changes on the ΔLGIIK9het25 chromosomes and across the genome and reasonably
409 explains gene activation in the NKL2 strain. Of course, altered promoters can also drive gene
410 expression changes, as observed by the insertion of the strong P_{trpC} promoter on LG II caused a
411 local increase in Hi-C contacts and the production of mRNA from gene NCU08696 proximal to
412 the LGIIK9het25 region. In fact, NCU08696, and others close to constitutive heterochromatic
413 regions, are downregulated in a Δ*dim-5* strain devoid of H3K9me3. Further, the proper expression

414 of the Neurospora *met-8* gene requires the immediately adjacent interspersed constitutive
415 heterochromatic region (54). Together, these data support a hypothetical role for constitutive
416 heterochromatin in regulating gene expression. In fact, the local deposition of H3K9me3 at a gene
417 promoter can repress gene expression in metazoans, as the control of mouse embryonic stem cell
418 identity requires the co-deposition of H3K9me3 and H3K36me3 for transcriptional repression
419 (55). Thus, in addition to the canonical repression of transposable elements and repetitive
420 sequences in eukaryotic genomes (56–59), H3K9me3 directly regulates gene transcription. We
421 propose heterochromatin-mediated gene regulation also occurs through 3D organization, where
422 genes interact with H3K9me3-enriched regions. Specifically, genes would associate with
423 constitutive heterochromatic regions to localize to the more repressive periphery for reducing
424 transcription, and should these genes move to the more active nuclear center, transcription would
425 increase. Currently, it is unknown how the constitutive heterochromatin – gene interaction occurs,
426 but aggregation of HP1 bound to H3K9me3 at promoters with the constitutive heterochromatin
427 bundle is an attractive model. Fungi may be more apt to employ this transcriptional regulation
428 mechanism, as opposed to their metazoan counterparts, given how fungal TAD-like structures have
429 more promiscuous contacts and how the Rabl chromosome conformation has extensive inter-
430 chromosomal contacts (9, 23–25, 35). Recently, the histone methyltransferase SETDB1, which
431 catalyzes H3K9me3 across metazoan genomes, was shown to maintain gene expression in addition
432 to driving chromatin compartmentalization (60), suggesting that constitutive heterochromatic
433 regions have additional, underappreciated roles in both genome organization and function across
434 diverse species. Further research in multiple species should help elucidate novel functional roles
435 for this "junk DNA" that is pervasive yet evolutionarily retained in genomes from fungi to
436 metazoans.

437

438 **Materials and Methods**

439 *Strains and growth conditions*

440 *Neurospora crassa* strains WT N150 (derived from the strain 74-OR23-IVA [Fungal Genetics
441 Stock Center #2489]), N2930 (*mat A his-3; Δmus52::bar*$^{+}$), N3944 (mat x; Δ*dim-5::bar*$^{+}$), and
442 N4933 (*mat a*; Δ47.4 kb::*hph*$^{+}$) were gifts from Eric U. Selker (University of Oregon). All strains
443 were grown with 1x Vogels minimal medium + 1.5% sucrose and supplements at 32ºC (61). All
444 strains are available upon request.

445 The ΔLGIIK9het25 (NKL2) strain replacing 110,609 basepairs (bp) of AT-rich DNA from
446 H3K9me3-enriched region #25 on LG II (between bp 3,602,033 and 3,712,857 of Neurospora
447 reference genome version 14 [nc14]) (23) with 1,401 bp of the P_{trpC}*::hph* hygromycin resistance
448 cassette (deleting a total of 109,208 bp of DNA from the Neurospora genome) was created by split
449 marker gene replacement. Briefly, the ~1,000 bp upstream of LGIIK9het25 was PCR amplified
450 with oligonucleotides ("oligos") oKL14 and oKL15, while the ~1,000 bp downstream of
451 LGIIK9het25 was amplified with oligos oKL18 and oKL19, by Phusion DNA polymerase (cat#
452 F530-L; ThermoFisher Scientific) using the manufacturer's conditions; oligos oKL15 and oKL18
453 had ten 5' complementary nucleotides specific to the P_{trpC} promoter and *hph* gene 3' end,
454 respectively. Oligo sequences are provided in Table S1. DNA fragments were gel purified using
455 the GenCatch Gel Extraction Kit (cat# 2260250; Epoch Life Sciences), and split marker fragments
456 fusing the LGIIK9het25 upstream to the P_{trpC} promoter ("UP"; oKL14 and 2955) or fusing the *hph*
457 gene to the LGIIK9het25 downstream ("DOWN"; oligos 2954 and oKL19) were PCR amplified
458 with the upstream and downstream fragments, and an *hph* gene containing plasmid
459 (p3xFLAG::hph::LoxP) (62) using LA Taq (cat# RR002M; Takara), and gel purified. The UP and

460 DOWN split marker fragments were transformed into N2930 by electroporation (BioRad
461 MicroPulser Electroporator, cat# 1652100EDU). Hygromycin resistant colonies were selected on
462 1x Vogels+FGS media with 100 µg/mL hygromycin (cat# ant-hg-5; Invivogen). Genomic DNA
463 was isolated from resultant colonies, using standard protocols (63), and proper hygromycin
464 cassette integration at LGIIK9het25 borders was performed by PCR using oKL49 and 2955 for
465 the left border, 2954 and oKL50 for the right border, and oKL49 and oKL50 for the entire
466 integrated P_{trpC}*::hph* gene. Positive integrant strain tKL1A-2 was crossed to N150 (xKL9AR) and
467 genomic DNA was isolated from hygromycin resistant progeny; similar PCR reactions were
468 performed to confirm the presence of the ΔLGIIK9het25 allele in individual cross progeny. PCR
469 with oligos oKL55 and oKL56 determined Δ*mus-52::bar* allele absence; strain mating type was
470 established by crosses with strains of known mating types. The final homokaryotic strain NKL2
471 from cross progeny xKL9AR-17 contains only the ΔLGIIK9het25 deletion (NKL2 genotype: *mat*
472 *A; ΔLGIIK9het25::hph*).
473
474 *Hi-C library construction and bioinformatic analyses*
475 *In situ* Hi-C was performed as previously described (23, 24). Hi-C libraries were Illumina
476 sequenced at the Genomics and Cell Characterization Core Facility (GC3F; University of Oregon),
477 either on a Hi-Seq 2500 as PE100 reads or a NovaSeq 6000 as PE59 reads. For comparison to
478 mutant Hi-C datasets, WT *Dpn*II and *Mse*I *in situ* Hi-C datasets (NCBI Gene Expresssion Omnibus
479 (GEO) accession number GSE173593) (23) were generated by extracting the number of total reads
480 from WT datasets using the sed command to provide approximately equal numbers of valid reads
481 as mutant datasets. Reads were mapped with bowtie2 (64) to the *Neurospora crassa* version 14
482 (nc14) reference genome (23), the output sam files were used to build the initial Hi-C contact

483 matrix at a high [1 kb] resolution with hicExplorer software package (65), and the output contact
484 matrix was used to analyze replicate dataset similarity (hicCorrelate), generate lower resolution
485 contact matrices (hicMergeMatrixBins), compare WT and mutant datasets (hicCompareMatrices),
486 KR correct matrices (hicCorrectMatrix), assess TADs (hicFindTADs [using --
487 correctForMultipleTesting false discovery rate, --thresholdComparisons 0.3, and --delta 0.15
488 values to make TAD bed files] and hicPlotTADs), and generate images (hicPlotMatrix). Individual
489 chromosome 3D structure prediction was performed with 3DMax (https://github.com/BDM-
490 Lab/3DMax)(45) while entire Neurospora 3D genome structure prediction was performed by
491 LorDG (66), both using custom scripts that are available on the Oluwadare lab GitHub website
492 (https://github.com/OluwadareLab/Fungi_3DGenome), tailored to fungal chromosome biology.
493 Input contact matrices for structure prediction were made by merging the individual *Dpn*II and
494 *Mse*I matrices (hicSumMatrices) and converting the .h5 output format to NxN text files with a
495 custom script (23) (https://github.com/Klocko-Lab). Output PDB files were displayed on
496 ChimeraX (67), individual bins with differentially expressed genes or chromosomal features were
497 manually colored, and high-resolution images were used for figure construction. PDB files are
498 available on Zenodo (10.5281/zenodo.11245552).
499
500 *Chromatin Immunoprecipitation-sequencing (ChIP-seq) library construction and bioinformatic*
501 *analyses*
502 ChIP-seq was performed as previously described (38), using anti-H3K9me3 (Active Motif;
503 cat# 39161, lot# 30220003) and anti-H3K27me2/3 (Active Motif; cat# 39535, lot# 23120014)
504 antibodies. All ChIP-seq libraries were Illumina sequenced at the GC3F on a NovaSeq 6000 as
505 SR118 reads. Fastq dataset files were mapped to nc14 with bowtie2 (64), converted to bam files,

506 sorted, and indexed with samtools (68), made into bigwig or bedgraph files with Deeptools (69),
507 and displayed on Integrative Genomics Viewer (IGV) (70), with exported png images from IGV
508 used for figure creation. Previously published NCBI GEO or the NCBI Sequence Read Archive
509 (SRA) datasets for WT H3K9me3 (GEO accession numbers GSE68897 and GSE98911), WT
510 H3K27me2/3 (GEO accession numbers GSE68897 and GSE100770), and Δ*dim-5* H3K27me2/3
511 (GEO accession number GSE68897 and SRA accession number SRP058573)(31, 46, 47, 71), were
512 mapped to the nc14 genome (23) and used for bigwig/bedgraph file creation for image generation.
513

514 *Total RNA isolation, polyadenylated RNA-seq library construction, and bioinformatic analyses*

515 Total RNA was isolated from overnight liquid cultures of Neurospora strains grown in 1x
516 Vogels, 1.5% sucrose plus supplements (32, 36). Cultures were harvested by vacuum filtration,
517 placed in 2.0mL screw-top tubes, and 300µL of acid washed glass beads suspended in dH_2O (150-
518 212µm, Sigma Aldrich cat# G1145-10G), 350µL Acid Phenol:chloroform (5:1; ThermoFisher cat#
519 AM9720), and 350µL NETS (300mM NaCl, 1mM EDTA, 10mM Tris pH 7.5, 0.2% SDS) were
520 added. Samples were vortexed for 10 minutes at maximum speed and centrifuged at 4ºC for 5
521 minutes at 13k rpm. The aqueous layer was transferred to two tubes (~250µL each), 650µL of cold
522 100% EtOH was added, and RNA was precipitated on ice for 10 minutes and pelleted by
523 microcentrifugation at 4ºC for 10 minutes at 13k rpm. The pellet was washed with cold 70% EtOH
524 (made with DECP-treated dH_2O), the supernatant was removed, and pellets were allowed to air
525 dry for 15 minutes and resuspended in 50µL DEPC-treated dH_2O. Insoluble material was removed
526 by centrifugation, and the initial RNA concentration was measured by Nanodrop. Total RNA
527 (10µg) was resuspended in 50µL of DEPC-treated dH_2O. Total RNA cleanup was performed by
528 the Zymo RNA clean and concentrator kit (Zymo Research cat# R1013), per the manufacturer's

529 protocol; the 15µL elution was divided into 4µL for Qubit concentration (RNA HS assay kit;
530 ThermoFisher Scientific, cat# Q32852) and TapeStation (Agilent) quality control analysis, while
531 the remaining 11µL was stored at -80oC. Only total RNA samples with high ribosomal RNA to
532 messenger RNA (mRNA) ratios were used for library construction. Polyadenylated mRNA (polyA
533 mRNA) was selected with the NEBNext Poly(A) mRNA Magnetic Isolation Module (New
534 England Biolabs [NEB], cat# E7490L) and polyA mRNA sequencing libraries were generated with
535 the NEBNext Ultra II Directional RNA Library Prep Kit for Illumina (NEB, cat# E7760L and
536 E7765L) per the manufacturer's protocols; quadruplicate polyA mRNA-seq replicate libraries
537 were constructed for each strain. All polyA mRNA-seq libraries were Illumina sequenced at the
538 GC3F on a NovaSeq 6000 as SR118 reads. Raw fastq files were mapped to the nc14 genome using
539 HiSat2 (72), and gene count files were generated with htseq-count (73). Differential Expression
540 analysis between strains was performed with DESeq2 (74) in R/Rstudio (75, 76), selecting
541 significantly changed genes as those with expression $\log_2 > 3.0$ or $\log_2 < -3.0$ and an adjusted p-
542 value < 0.001; bed files for display on IGV were generated from the DESeq2 output gene lists in
543 Microsoft Excel, and volcano plots of $\log_2$ fold change vs. adjusted p-value were generated in R/R
544 studio.
545
546 **Data Availability**
547 All genomic datasets have been deposited to the NCBI GEO under the SuperSeries accession
548 number GSE269235. Individual datasets have the subseries numbers GSE269228 (ChIP-seq),
549 GSE269229 (Hi-C), and GSE269230 (polyA mRNA-seq).
550
551 **Acknowledgements**

The authors thank Sara Rodriguez, Yulia Shtanko, and Ashley Scadden for Hi-C library generation help; Sara Hanson (Colorado College) for TapeStation use and RNA-seq protocol advice; the University of Oregon GC3F for Illumina library sequencing service, and Klocko lab members and UCCS Department of Chemistry & Biochemistry colleagues for helpful comments and discussions. Funding was provided by a UCCS Undergraduate Research Academy award to A.T.R., start-up funds from the UCCS College of Engineering and Applied Science to O.O., a Maximizing Investigators Research Award grant (1R35GM150402-01) to O.O., start-up funds from the UCCS College of Letters, Arts, and Sciences to A.D.K., and a NIH Academic Research Enhancement Award grant (1R15GM140396-01) to A.D.K.

Declaration of Interest Statement

The authors report there are no competing interests to declare.

References

1. Cremer T, Cremer C. 2001. Chromosome territories, nuclear architecture and gene regulation in mammalian cells. Nat Rev Genet 2:292–301.

2. Misteli T. 2007. Beyond the Sequence: Cellular Organization of Genome Function. Cell 128:787–800.

3. Dekker J. 2008. Gene Regulation in the Third Dimension. Science 319:1793–1794.

4. Sexton T, Cavalli G. 2015. The Role of Chromosome Domains in Shaping the Functional Genome. Cell 160:1049–1059.

5. Bonev B, Cavalli G. 2016. Organization and function of the 3D genome. Nat Rev Genet 17:661–678.

6. Flavahan WA, Drier Y, Liau BB, Gillespie SM, Venteicher AS, Stemmer-Rachamimov AO, Suvà ML, Bernstein BE. 2016. Insulator dysfunction and oncogene activation in IDH mutant gliomas. Nature 529:110–114.

7. Dixon JR, Xu J, Dileep V, Zhan Y, Song F, Le VT, Yardımcı GG, Chakraborty A, Bann DV, Wang Y, Clark R, Zhang L, Yang H, Liu T, Iyyanki S, An L, Pool C, Sasaki T, Rivera-Mulia JC, Ozadam H, Lajoie BR, Kaul R, Buckley M, Lee K, Diegel M, Pezic D, Ernst C, Hadjur S, Odom DT, Stamatoyannopoulos JA, Broach JR, Hardison RC, Ay F, Noble WS, Dekker J, Gilbert DM, Yue F. 2018. Integrative detection and analysis of structural variation in cancer genomes. Nat Genet 50:1388–1398.

8. Northcott PA, Lee C, Zichner T, Stütz AM, Erkek S, Kawauchi D, Shih DJH, Hovestadt V, Zapatka M, Sturm D, Jones DTW, Kool M, Remke M, Cavalli FMG, Zuyderduyn S, Bader GD, VandenBerg S, Esparza LA, Ryzhova M, Wang W, Wittmann A, Stark S, Sieber L, Seker-Cin H, Linke L, Kratochwil F, Jäger N, Buchhalter I, Imbusch CD, Zipprich G, Raeder B, Schmidt S, Diessl N, Wolf S, Wiemann S, Brors B, Lawerenz C, Eils J, Warnatz H-J, Risch T, Yaspo M-L, Weber UD, Bartholomae CC, Kalle C von, Turányi E, Hauser P, Sanden E, Darabi A, Siesjö P, Sterba J, Zitterbart K, Sumerauer D, Sluis P van, Versteeg R, Volckmann R, Koster J, Schuhmann MU, Ebinger M, Grimes HL, Robinson GW, Gajjar A, Mynarek M, Hoff K von, Rutkowski S, Pietsch T, Scheurlen W, Felsberg J, Reifenberger G, Kulozik AE, Deimling A von, Witt O, Eils R, Gilbertson RJ, Korshunov A, Taylor MD, Lichter P, Korbel JO, Wechsler-Reya RJ, Pfister SM. 2014. Enhancer hijacking activates GFI1 family oncogenes in medulloblastoma. Nature 511:428–34.

9. Torres DE, Reckard AT, Klocko AD, Seidl MF. 2023. Nuclear genome organization in fungi: From gene folding to Rabl chromosomes. FEMS Microbiol Rev https://doi.org/10.1093/femsre/fuad021.

10. Rao SSP, Huntley MH, Durand NC, Stamenova EK, Bochkov ID, Robinson JT, Sanborn AL, Machol I, Omer AD, Lander ES, Aiden EL. 2014. A 3D Map of the Human Genome at Kilobase Resolution Reveals Principles of Chromatin Looping. Cell 159:1665–1680.

11. Lieberman-Aiden E, Berkum NL van, Williams L, Imakaev M, Ragoczy T, Telling A, Amit I, Lajoie BR, Sabo PJ, Dorschner MO, Sandstrom R, Bernstein B, Bender MA, Groudine M, Gnirke A, Stamatoyannopoulos J, Mirny LA, Lander ES, Dekker J. 2009. Comprehensive Mapping of Long-Range Interactions Reveals Folding Principles of the Human Genome. Science 326:289–293.

12. Luger K, Mäder AW, Richmond RK, Sargent DF, Richmond TJ. 1997. Crystal structure of the nucleosome core particle at 2.8 Å resolution. Nature 389:251–260.

13. Luger K, Richmond TJ. 1998. DNA binding within the nucleosome core. Curr Opin Struc Biol 8:33–40.

14. Rao SSP, Huang S-C, Hilaire BGS, Engreitz JM, Perez EM, Kieffer-Kwon K-R, Sanborn AL, Johnstone SE, Bascom GD, Bochkov ID, Huang X, Shamim MS, Shin J, Turner D, Ye Z, Omer AD, Robinson JT, Schlick T, Bernstein BE, Casellas R, Lander ES, Aiden EL. 2017. Cohesin Loss Eliminates All Loop Domains. Cell 171:305-320.e24.

15. Mizuguchi T, Fudenberg G, Mehta S, Belton J-M, Taneja N, Folco HD, FitzGerald P, Dekker J, Mirny L, Barrowman J, Grewal SIS. 2014. Cohesin-dependent globules and heterochromatin shape 3D genome architecture in *S. pombe*. Nature 516:432–435.

16. Campos EI, Reinberg D. 2009. Histones: Annotating Chromatin. Annu Rev Genet 43:559–599.

17. Dixon JR, Selvaraj S, Yue F, Kim A, Li Y, Shen Y, Hu M, Liu JS, Ren B. 2012. Topological Domains in Mammalian Genomes Identified by Analysis of Chromatin Interactions. Nature 485:376–380.

18. Kind J, Pagie L, de Vries SS, Nahidiazar L, Dey SS, Bienko M, Zhan Y, Lajoie B, de Graaf CA, Amendola M, Fudenberg G, Imakaev M, Mirny LA, Jalink K, Dekker J, van Oudenaarden A, van Steensel B. 2015. Genome-wide Maps of Nuclear Lamina Interactions in Single Human Cells. Cell 163:134–147.

19. Falk M, Feodorova Y, Naumova N, Imakaev M, Lajoie BR, Leonhardt H, Joffe B, Dekker J, Fudenberg G, Solovei I, Mirny LA. 2019. Heterochromatin drives compartmentalization of inverted and conventional nuclei. Nature 570:395–399.

20. Schoenfelder S, Sexton T, Chakalova L, Cope NF, Horton A, Andrews S, Kurukuti S, Mitchell JA, Umlauf D, Dimitrova DS, Eskiw CH, Luo Y, Wei C-L, Ruan Y, Bieker JJ, Fraser P. 2010. Preferential associations between co-regulated genes reveal a transcriptional interactome in erythroid cells. Nat Genet 42:53–61.

21. Hoencamp C, Dudchenko O, Elbatsh AMO, Brahmachari S, Raaijmakers JA, Schaik T van, Cacciatore ÁS, Contessoto VG, Heesbeen RGHP van, Broek B van den, Mhaskar AN, Teunissen H, Hilaire BGS, Weisz D, Omer AD, Pham M, Colaric Z, Yang Z, Rao SSP, Mitra N, Lui C, Yao W, Khan R, Moroz LL, Kohn A, Leger JSt, Mena A, Holcroft K, Gambetta MC, Lim F, Farley E, Stein N, Haddad A, Chauss D, Mutlu AS, Wang MC, Young ND, Hildebrandt E, Cheng HH, Knight CJ, Burnham TLU, Hovel KA, Beel AJ, Mattei P-J, Kornberg RD, Warren WC, Cary G, Gómez-Skarmeta JL, Hinman V, Lindblad-Toh K, Palma FD, Maeshima K, Multani AS, Pathak S, Nel-Themaat L, Behringer RR, Kaur P, Medema RH, Steensel B van, Wit E de, Onuchic JN, Pierro MD, Aiden EL, Rowland BD. 2021. 3D genomics across the tree of life reveals condensin II as a determinant of architecture type. Science 372:984–989.

22. Imakaev M, Fudenberg G, McCord RP, Naumova N, Goloborodko A, Lajoie BR, Dekker J, Mirny LA. 2012. Iterative correction of Hi-C data reveals hallmarks of chromosome organization. Nat Methods 9:999–1003.

23. Rodriguez S, Ward A, Reckard AT, Shtanko Y, Hull-Crew C, Klocko AD. 2022. The genome organization of *Neurospora crassa* at high resolution uncovers principles of fungal chromosome topology. G3 Genes Genomes Genetics https://doi.org/10.1093/g3journal/jkac053.

24. Galazka JM, Klocko AD, Uesaka M, Honda S, Selker EU, Freitag M. 2016. Neurospora chromosomes are organized by blocks of importin alpha-dependent heterochromatin that are largely independent of H3K9me3. Genome Res 26:1069–1080.

25. Torres DE, Kramer HM, Tracanna V, Fiorin GL, Cook DE, Seidl MF, Thomma BPHJ. 2023. Implications of the three-dimensional chromatin organization for genome evolution in a fungal plant pathogen. Nat Commun 15:1701.

26. Galagan JE, Calvo SE, Borkovich KA, Selker EU, Read ND, Jaffe D, FitzHugh W, Ma L-J, Smirnov S, Purcell S, Rehman B, Elkins T, Engels R, Wang S, Nielsen CB, Butler J, Endrizzi M, Qui D, Ianakiev P, Bell-Pedersen D, Nelson MA, Werner-Washburne M, Selitrennikoff CP, Kinsey JA, Braun EL, Zelter A, Schulte U, Kothe GO, Jedd G, Mewes W, Staben C, Marcotte E, Greenberg D, Roy A, Foley K, Naylor J, Stange-Thomann N, Barrett R, Gnerre S, Kamal M, Kamvysselis M, Mauceli E, Bielke C, Rudd S, Frishman D, Krystofova S, Rasmussen C, Metzenberg RL, Perkins DD, Kroken S, Cogoni C, Macino G, Catcheside D, Li W, Pratt RJ, Osmani SA, DeSouza CPC, Glass L, Orbach MJ, Berglund JA, Voelker R, Yarden O, Plamann M, Seiler S, Dunlap J, Radford A, Aramayo R, Natvig DO, Alex LA, Mannhaupt G, Ebbole DJ, Freitag M, Paulsen I, Sachs MS, Lander ES, Nusbaum C, Birren B. 2003. The genome sequence of the filamentous fungus *Neurospora crassa*. Nature 422:859–868.

27. Lewis ZA, Honda S, Khlafallah TK, Jeffress JK, Freitag M, Mohn F, Schübeler D, Selker EU. 2009. Relics of repeat-induced point mutation direct heterochromatin formation in *Neurospora crassa*. Genome Res 19:427–437.

28. Nurk S, Koren S, Rhie A, Rautiainen M, Bzikadze AV, Mikheenko A, Vollger MR, Altemose N, Uralsky L, Gershman A, Aganezov S, Hoyt SJ, Diekhans M, Logsdon GA, Alonge M, Antonarakis SE, Borchers M, Bouffard GG, Brooks SY, Caldas GV, Chen N-C, Cheng H, Chin C-S, Chow W, Lima LG de, Dishuck PC, Durbin R, Dvorkina T, Fiddes IT, Formenti G, Fulton RS, Fungtammasan A, Garrison E, Grady PGS, Graves-Lindsay TA, Hall IM, Hansen NF, Hartley GA, Haukness M, Howe K, Hunkapiller MW, Jain C, Jain M, Jarvis ED, Kerpedjiev P, Kirsche M, Kolmogorov M, Korlach J, Kremitzki M, Li H, Maduro VV, Marschall T, McCartney AM, McDaniel J, Miller DE, Mullikin JC, Myers EW, Olson ND, Paten B, Peluso P, Pevzner PA, Porubsky D, Potapova T, Rogaev EI, Rosenfeld JA, Salzberg SL, Schneider VA, Sedlazeck FJ, Shafin K, Shew CJ, Shumate A, Sims Y, Smit AFA, Soto DC, Sović I, Storer JM, Streets A, Sullivan BA, Thibaud-Nissen F, Torrance J, Wagner J, Walenz BP, Wenger A, Wood JMD, Xiao C, Yan SM, Young AC, Zarate S, Surti U, McCoy RC, Dennis MY, Alexandrov IA, Gerton JL, O'Neill RJ, Timp W, Zook JM, Schatz MC, Eichler EE, Miga KH, Phillippy AM. 2022. The complete sequence of a human genome. Science 376:44–53.

29. Tamaru H, Zhang X, McMillen D, Singh PB, Nakayama J, Grewal SI, Allis CD, Cheng X, Selker EU. 2003. Trimethylated lysine 9 of histone H3 is a mark for DNA methylation in *Neurospora crassa*. Nat Genet 34:75–79.

30. Lewis ZA, Adhvaryu KK, Honda S, Shiver AL, Knip M, Sack R, Selker EU. 2010. DNA Methylation and Normal Chromosome Behavior in Neurospora Depend on Five Components of a Histone Methyltransferase Complex, DCDC. Plos Genet 6:e1001196.

31. Klocko AD, Uesaka M, Ormsby T, Rountree MR, Wiles ET, Adhvaryu KK, Honda S, Selker EU. 2019. Nucleosome Positioning by an Evolutionarily Conserved Chromatin Remodeler Prevents Aberrant DNA Methylation in Neurospora. Genetics 211:563–578.

32. Jamieson K, Rountree MR, Lewis ZA, Stajich JE, Selker EU. 2013. Regional control of histone H3 lysine 27 methylation in Neurospora. Proc National Acad Sci 110:6027–6032.

33. Jamieson K, McNaught KJ, Ormsby T, Leggett NA, Honda S, Selker EU. 2018. Telomere repeats induce domains of H3K27 methylation in Neurospora. Elife 7:e31216.

34. Wiles ET, Selker EU. 2017. H3K27 methylation: a promiscuous repressive chromatin mark. Curr Opin Genet Dev 43:31–37.

35. Winter DJ, Ganley ARD, Young CA, Liachko I, Schardl CL, Dupont P-Y, Berry D, Ram A, Scott B, Cox MP. 2018. Repeat elements organise 3D genome structure and mediate transcription in the filamentous fungus *Epichloë festucae*. Plos Genet 14:e1007467.

36. Klocko AD, Ormsby T, Galazka JM, Leggett NA, Uesaka M, Honda S, Freitag M, Selker EU. 2016. Normal chromosome conformation depends on subtelomeric facultative heterochromatin in *Neurospora crassa*. Proc National Acad Sci 113:15048–15053.

37. Knight PA, Ruiz D. 2013. A fast algorithm for matrix balancing. Ima J Numer Anal 33:1029–1047.

38. Scadden AW, Graybill AS, Hull-Crew C, Lundberg TJ, Lande NM, Klocko AD. 2023. Histone deacetylation and cytosine methylation compartmentalize heterochromatic regions in the genome organization of *Neurospora crassa*. Proc Natl Acad Sci 120:e2311249120.

39. Ninomiya Y, Suzuki K, Ishii C, Inoue H. 2004. Highly efficient gene replacements in Neurospora strains deficient for nonhomologous end-joining. P Natl Acad Sci Usa 101:12248–12253.

40. Selker E. 1990. Premeiotic Instability Of Repeated Sequences In *Neurospora crassa*. Annu Rev Genet 24:579–613.

41. Gladyshev E, Kleckner N. 2014. Direct recognition of homology between double helices of DNA in *Neurospora crassa*. Nat Commun 5:3509–3509.

42. Bonhoure N, Bounova G, Bernasconi D, Praz V, Lammers F, Canella D, Willis IM, Herr W, Hernandez N, Delorenzi M, Consortium TC, Hernandez N, Delorenzi M, Deplancke B, Desvergne B, Guex N, Herr W, Naef F, Rougemont J, Schibler U, Andersin T, Cousin P, Gilardi F, Gos P, Lammers F, Raghav S, Villeneuve D, Fabbretti R, Vlegel V, Xenarios I, Migliavacca E, Praz V, David F, Jarosz Y, Kuznetsov D, Liechti R, Martin O, Delafontaine J, Cajan J, Gustafson K, Krier I, Leleu M, Molina N, Naldi A, Rib L, Symul L, Bounova G. 2014. Quantifying ChIP-seq data: a spiking method providing an internal reference for sample-to-sample normalization. Genome Res 24:1157–68.

43. Orlando DA, Chen MW, Brown VE, Solanki S, Choi YJ, Olson ER, Fritz CC, Bradner JE, Guenther MG. 2014. Quantitative ChIP-Seq Normalization Reveals Global Modulation of the Epigenome. Cell Reports 9:1163–1170.

44. Zufferey M, Tavernari D, Oricchio E, Ciriello G. 2018. Comparison of computational methods for the identification of topologically associating domains. Genome Biol 19:217.

45. Oluwadare O, Zhang Y, Cheng J. 2018. A maximum likelihood algorithm for reconstructing 3D structures of human chromosomes from chromosomal contact data. BMC Genom 19:161.

46. Jamieson K, Wiles ET, McNaught KJ, Sidoli S, Leggett N, Shao Y, Garcia BA, Selker EU. 2016. Loss of HP1 causes depletion of H3K27me3 from facultative heterochromatin and gain of H3K27me2 at constitutive heterochromatin. Genome Res 26:97–107.

47. Basenko EY, Sasaki T, Ji L, Prybol CJ, Burckhardt RM, Schmitz RJ, Lewis ZA. 2015. Genome-wide redistribution of H3K27me3 is linked to genotoxic stress and defective growth. Proc National Acad Sci 112:E6339–E6348.

48. Poinsignon T, Gallopin M, Grognet P, Malagnac F, Lelandais G, Poulain P. 2023. 3D models of fungal chromosomes to enhance visual integration of omics data. NAR Genom Bioinform 5:lqad104.

49. Connolly LR, Smith KM, Freitag M. 2013. The Fusarium graminearum Histone H3 K27 Methyltransferase KMT6 Regulates Development and Expression of Secondary Metabolite Gene Clusters. Plos Genet 9:e1003916.

50. Larson AG, Elnatan D, Keenen MM, Trnka MJ, Johnston JB, Burlingame AL, Agard DA, Redding S, Narlikar GJ. 2017. Liquid droplet formation by HP1α suggests a role for phase separation in heterochromatin. Nature 547:236–240.

51. Freitag M, Hickey PC, Khlafallah TK, Read ND, Selker EU. 2004. HP1 Is Essential for DNA Methylation in Neurospora. Mol Cell 13:427–434.

52. Zenk F, Zhan Y, Kos P, Löser E, Atinbayeva N, Schächtle M, Tiana G, Giorgetti L, Iovino N. 2021. HP1 drives *de novo* 3D genome reorganization in early Drosophila embryos. Nature 593:289–293.

53. Stutzman AV, Hill CA, Armstrong RL, Gohil R, Duronio RJ, Dowen JM, McKay DJ. 2024. Heterochromatic 3D genome organization is directed by HP1a- and H3K9-dependent and independent mechanisms. Mol Cell https://doi.org/10.1016/j.molcel.2024.05.002.

54. Yang S, Li W, Qi S, Gai K, Chen Y, Suo J, Cao Y, He Y, Wang Y, He Q. 2014. The highly expressed methionine synthase gene of *Neurospora crassa* is positively regulated by its proximal heterochromatic region. Nucleic Acids Res 42:6183–95.

55. Barral A, Pozo G, Ducrot L, Papadopoulos GL, Sauzet S, Oldfield AJ, Cavalli G, Déjardin J. 2022. SETDB1/NSD-dependent H3K9me3/H3K36me3 dual heterochromatin maintains gene expression profiles by bookmarking poised enhancers. Mol Cell 82:816-832.e12.

56. Padeken J, Zeller P, Towbin B, Katic I, Kalck V, Methot SP, Gasser SM. 2019. Synergistic lethality between BRCA1 and H3K9me2 loss reflects satellite derepression. Genes Dev 33:436–451.

57. Padeken J, Methot SP, Gasser SM. 2022. Establishment of H3K9-methylated heterochromatin and its functions in tissue differentiation and maintenance. Nat Rev Mol Cell Biol 23:623–640.

58. Herberg S, Simeone A, Oikawa M, Jullien J, Bradshaw CR, Teperek M, Gurdon J, Miyamoto K. 2015. Histone H3 lysine 9 trimethylation is required for suppressing the expression of an embryonically activated retrotransposon in *Xenopus laevis*. Sci Rep 5:14236.

59. Zhao S, Lu J, Pan B, Fan H, Byrum SD, Xu C, Kim A, Guo Y, Kanchi KL, Gong W, Sun T, Storey AJ, Burkholder NT, Mackintosh SG, Kuhlers PC, Edmondson RD, Strahl BD, Diao Y, Tackett AJ, Raab JR, Cai L, Song J, Wang GG. 2023. TNRC18 engages H3K9me3 to mediate silencing of endogenous retrotransposons. Nature 623:633–642.

60. Keenan CR, Coughlan HD, Iannarella N, Fierro AT del, Keniry A, Johanson TM, Chan WF, Garnham AL, Whitehead LW, Blewitt ME, Smyth GK, Allan RS. 2024. Suv39h-catalyzed H3K9me3 is critical for euchromatic genome organization and the maintenance of gene transcription. Genome Res 34:556–571.

61. Davis RH. 2000. Neurospora: contributions of a model organism. Oxford University Press.

62. Honda S, Selker EU. 2009. Tools for Fungal Proteomics: Multifunctional Neurospora Vectors for Gene Replacement, Protein Expression and Protein Purification. Genetics 182:11–23.

63. Miao VPW, Freitag M, Selker EU. 2000. Short TpA-rich segments of the ζ-η region induce DNA methylation in *Neurospora crassa.* J Mol Biol 300:249–273.

64. Langmead B, Salzberg SL. 2012. Fast gapped-read alignment with Bowtie 2. Nat Methods 9:357–359.

65. Ramírez F, Bhardwaj V, Arrigoni L, Lam KC, Grüning BA, Villaveces J, Habermann B, Akhtar A, Manke T. 2018. High-resolution TADs reveal DNA sequences underlying genome organization in flies. Nat Commun 9:189.

66. Trieu T, Cheng J. 2017. 3D genome structure modeling by Lorentzian objective function. Nucleic Acids Res 45:1049–1058.

67. Pettersen EF, Goddard TD, Huang CC, Meng EC, Couch GS, Croll TI, Morris JH, Ferrin TE. 2021. UCSF ChimeraX: Structure visualization for researchers, educators, and developers. Protein Sci 30:70–82.

68. Li H, Handsaker B, Wysoker A, Fennell T, Ruan J, Homer N, Marth G, Abecasis G, Durbin R, Subgroup 1000 Genome Project Data Processing. 2009. The Sequence Alignment/Map format and SAMtools. Bioinformatics 25:2078–2079.

69. Ramírez F, Ryan DP, Grüning B, Bhardwaj V, Kilpert F, Richter AS, Heyne S, Dündar F, Manke T. 2016. deepTools2: a next generation web server for deep-sequencing data analysis. Nucleic Acids Res 44:W160-5.

70. Robinson JT, Thorvaldsdóttir H, Winckler W, Guttman M, Lander ES, Getz G, Mesirov JP. 2011. Integrative genomics viewer. Nat Biotechnol 29:24–6.

71. Klocko AD, Summers CA, Glover ML, Parrish R, Storck WK, McNaught KJ, Moss ND, Gotting K, Stewart A, Morrison AM, Payne L, Hatakeyama S, Selker EU. 2020. Selection and Characterization of Mutants Defective in DNA Methylation in *Neurospora crassa*. Genetics 216:genetics.303471.2020.

72. Zhang Y, Park C, Bennett C, Thornton M, Kim D. 2020. Rapid and accurate alignment of nucleotide conversion sequencing reads with HISAT-3N. Genome Res 31:1290–1295.

73. Anders S, Pyl PT, Huber W. 2015. HTSeq--a Python framework to work with high-throughput sequencing data. Bioinform Oxf Engl 31:166–9.

74. Love MI, Huber W, Anders S. 2014. Moderated estimation of fold change and dispersion for RNA-seq data with DESeq2. Genome Biol 15:550.

75. Team Rs. 2020. RStudio: Integrated Development for R. RStudio, PBC, Boston, MA. http://www.rstudio.com/.

76. Team RC. 2021. R: A language and environment for statistical computing. R Foundation for Statistical Computing, Vienna, Austria. https://www.R-project.org/.

Figure Legends

Figure 1. A strain harboring a 47.4 kilobase deletion of a H3K27me2/3-enriched domain has minimal genome organization change. (A-B) Contact probability heatmaps of *Dpn*II (euchromatin-specific) *in situ* Hi-C datasets at 20 kb resolution across Linkage Group VI (LG VI) of the (A) wild type (WT) or (B) N4933 strains, the latter deleted of a Δ47.4kb H3K27me2/3-enriched region ("ΔK27"). Enhanced heatmaps show the terminal 500 kb of LG VI, harboring the deleted H3K27me2/3 region, at 5 kb resolution. Each Hi-C image displayed has the raw contact

822 probability heatmap shown above the diagonal and the Knight Ruiz (KR) corrected contact
823 probability heatmap, for reducing inherent contact probability biases (37), displayed below the
824 diagonal. Contact probability scale bars shown below the images. Images of wild type H3K9me3
825 (green) and H3K27me2/3 (purple) ChIP-seq tracks, displayed on IGV (70), above and to the right.
826 The purple line in (A) shows the WT location of the H3K27me2/3-enriched region that was deleted
827 in the ΔK27 strain, while the black arrowhead in (B) shows the deletion site in the N4933 strain.
828 (C) KR corrected contact probability heatmaps of the *Dpn*II *in situ* Hi-C datasets of WT and ΔK27
829 strains primarily showing on-diagonal contacts at 5 kb bin resolution. Wild type H3K9me3 ChIP-
830 seq (green), H3K27me2/3 ChIP-seq (purple), and gene (gray) tracks shown below. Contact
831 probability scalebar to the left. The black arrowhead shows the gain in contacts between fused
832 euchromatic DNA flanking the ΔK27 deletion. The gray arrowhead shows a loss of contact
833 probability at a putative transposable element (gene NCU09969; *sly-1*). (D-E) Contact probability
834 heatmaps of telomere interactions within WT and ΔK27 strains, as (D) shows intra-chromosomal
835 (e.g., the contacts between the left and right telomeres of LG VI), while (E) shows inter-
836 chromosomal (e.g., the contacts between the left telomere of LG VI and the right telomere of LG
837 V) telomere contacts. Telomere schematic, with green circle showing the position of the telomere
838 repeats, H3K27me2/3 ChIP-seq (purple), and gene (gray) tracks shown above and to the right. The
839 red "X" shows the H3K27me2/3 domain that is deleted, while the black arrowhead shows the
840 depletion of contacts at that deletion site.
841
842 **Figure 2. Deletion of a ~110 kb H3K9me3-enriched domain alters constitutive**
843 **heterochromatic region clustering.** (A-D) Contact probability heatmaps of (A-B) *Dpn*II
844 (euchromatin-specific) and (C-D) *Mse*I (heterochromatin specific) *in situ* Hi-C datasets at 20 kb

845 resolution across LG II, , as in Figure 1A-B, of the (A, C) wild type (WT) or (B, D) NKL2 strains,
846 the latter deleted of the 25th H3K9me3-enriched region from the LG II left telomere
847 ("ΔLGIIK9het25"). The purple line on panel A shows the deleted LGIIK9het25 region. Enhanced
848 heatmaps at 5 kb resolution show a 500 kb region of LG II surrounding the ΔLGIIK9het25 allele,
849 as in Figure 1A-B. (E-F) Images showing the $\log_2$ change in Hi-C contact probability between WT
850 and ΔLGIIK9het25 (E) *Dpn*II (euchromatin-specific) or (F) *Mse*I (heterochromatin-specific)
851 datasets at 5 kb resolution across a 500 kb region of LG II surrounding the ΔLGIIK9het25 allele.
852 Scalebar of contact probability changes is shown below. (G) Images showing the change in inter-
853 chromosomal *Mse*I (heterochromatin-specific) Hi-C contact probability between the entire LG I
854 chromosome and the (top) LG II centromere or (bottom) LGIIK9het25 interspersed
855 heterochromatic region.
856
857 **Figure 3. The LGIIK9het25 deletion does not compromise the deposition of H3K9me3 at**
858 **other gene-poor constitutive heterochromatic regions in the NKL2 strain.** (A-B) Images of
859 WT (dark green) or NKL2 ΔLGIIK9het25 (light green) H3K9me3 ChIP-seq and gene (gray)
860 tracks, displayed on IGV, of the entire LG II chromosome or enhanced regions. H3K9me3 ChIP-
861 seq reads were mapped to the (A) WT nc14 reference genome or (B) the NKL2 ΔLGIIK9het25
862 reference genome. Numbers in the enhanced panel in Figure 3A count the heterochromatic regions
863 from the LG II left telomere, while the black arrowheads show the position at which the DNA
864 sequence has been deleted in the NKL2 ΔLGIIK9het25 strain, and the purple line shows the ~110
865 kb of DNA that is missing from the NKL2 genome (causing all peaks to be shifted by ~110 kb
866 starting at the black arrowhead). The red arrow in panel B shows the position of the inserted
867 P_{trpC}*::hph* gene in the NKL2 reference genome.

868

869 **Figure 4. The LGIIK9het25 deletion alters the predicted TAD-like structures in the**
870 **surrounding chromatin.** (A-B) Contact probability heatmaps of *Dpn*II (KR corrected) or *Mse*I
871 (raw) *in situ* Hi-C datasets of WT and ΔLGIIK9het25 strains primarily showing on-diagonal
872 contacts at 5 kb bin resolution, mapped to either the (A) nc14 WT reference genome or the (B)
873 NKL2 ΔLGIIK9het25 reference genome. Wild type H3K9me3 ChIP-seq (green) and gene (gray)
874 tracks shown below. The contact probability scalebar is shown to the left of each heatmap. Black
875 triangular lines show predicted TAD-like structures, as calculated by the program hicFindTADs,
876 in the defined regions. In panel B, the black arrowheads indicate predicted TAD-like structures
877 surrounding the LGIIK9het25 constitutive heterochromatic region deletion that change, while the
878 open arrowheads show altered TAD-like structures in more distant, flanking euchromatin. The red
879 arrow shows the position of the P_{trpC}*::hph* gene in the NKL2 reference genome, while the purple
880 line shows increased chromatin contacts surrounding the P_{trpC} promoter.

881

882 **Figure 5. The predicted 3D folding of a single chromosome is changed with the LGIIK9het25**
883 **deletion.** (A-B) Images depicting the predicted 3D modeling of LG II from (A) WT or (B) NKL2
884 ΔLGIIK9het25 strains at 20 kb resolution. The green highlighted region shows the 20 kb bins
885 covering the LGIIK9het25 region in the WT structure. The enhanced image shows the folding of
886 the chromatin at the right arm of LG II surrounding the LGIIK9het25 region in a WT strain. The
887 arrow shows the LGIIK9het25 deletion location.

888

889 **Figure 6. The LGIIK9het25 region deletion causes increased gene expression genome wide.**
890 (A) Volcano plots showing the $\log_2$ fold change from WT expression level of all Neurospora genes

891 verses adjusted p-values from (left) the NKL2 ΔLGIIK9het25 strain or (right) the Δ*dim-5* strain.
892 Points colored red are genes that have significant expression changes, with $\log_2$ fold changes > 3.0
893 or < -3.0 and adjusted p-values < 0.001. The number of significantly changed genes in each strain
894 indicated in red at the top of the plot. (B) Images of IGV tracks showing WT H3K9me3 ChIP-seq
895 (green), genes (gray), or the positions of differentially expressed genes with $\log_2$ fold changes >
896 3.0 ("up" genes) or < -3.0 ("down" genes) and adjusted p-values < 0.001. The purple "X" symbols
897 show the LGIIK9het25 constitutive heterochromatic region deleted in the NKL2 strain, while the
898 black arrows show the positions of genes NCU08696 on LG II or *dim-5* (NCU04402) on LG IV.
899 (C-D) Images depicting the predicted 3D modeling of LG II from (C) WT or (D) NKL2
900 ΔLGIIK9het25 strains at 20 kb resolution. The green highlighted region shows the 20 kb bins
901 encompassing the LGIIK9het25 region in the WT structure, while red highlights show the 20 kb
902 bins containing differentially expressed genes in the NKL2 strain, relative to a WT strain; the same
903 bins are marked on both structures. The arrow in panel D shows the LGIIK9het25 deletion
904 location.
905
906 **Figure 7. The predicted 3D structure of the entire genome, as well as the positions of**
907 **differentially expressed genes, are altered when the LGIIK9het25 region is deleted.** (A-B)
908 Images depicting the predicted 3D modeling of the entire genome of (A) WT or (B) NKL2
909 ΔLGIIK9het25 strains. The model on the left shows the side view of the genome structure, which
910 is rotated up 90° to obtain the right model, which shows the bottom of the structure from the
911 centromere cluster. The green highlighted region shows the 20 kb bins covering the LGIIK9het25
912 region in the WT structure, while the red regions highlight the 20 kb bins containing differentially
913 expressed genes in the NKL2 ΔLGIIK9het25 strain.

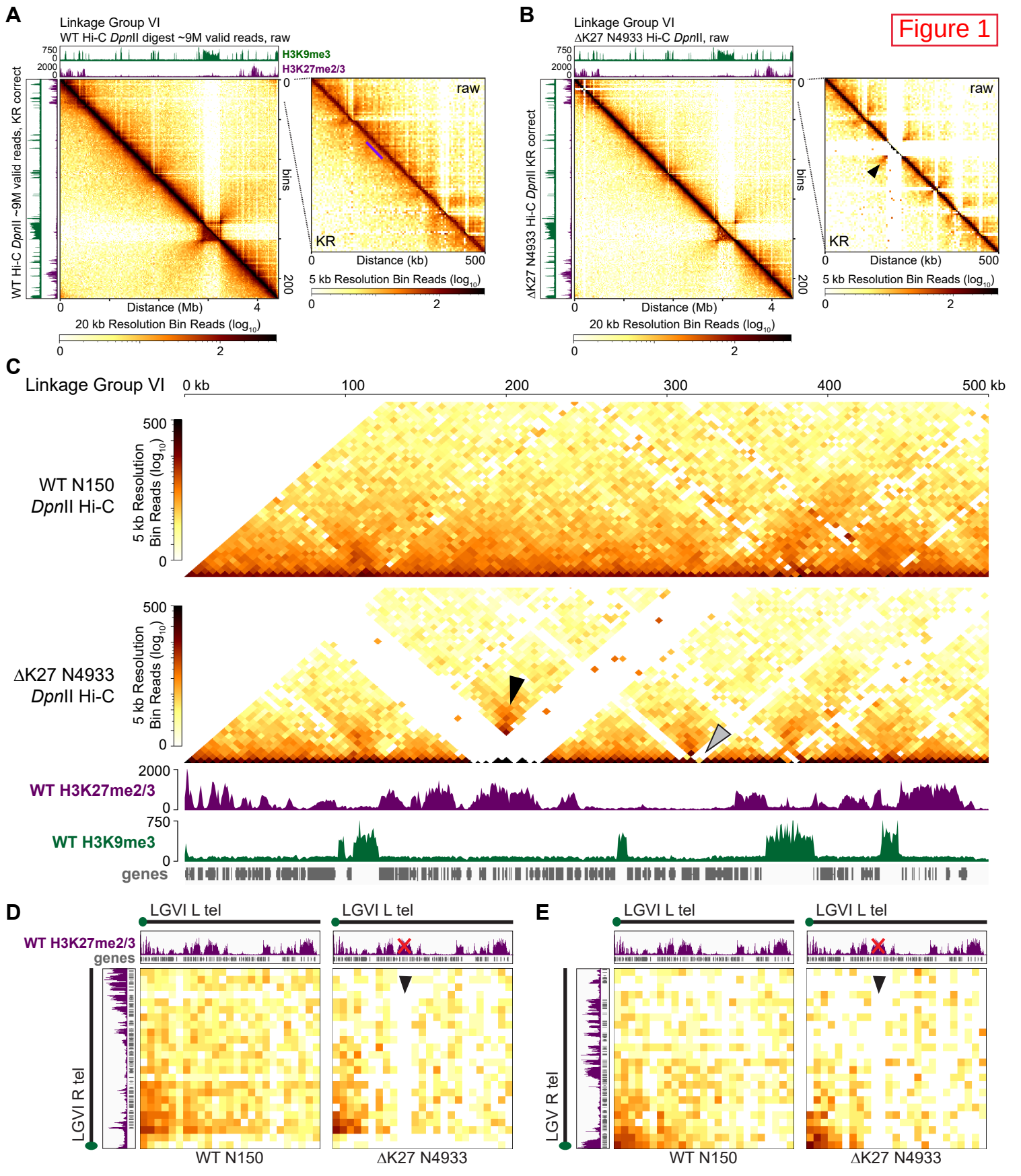
Figure 1
A
Linkage Group VI
WT Hi-C DpnII digest ~9M valid reads, raw
H3K9me3
H3K27me2/3
WT Hi-C DpnII ~9M valid reads, KR correct
raw
KR
bins
Distance (Mb)
Distance (kb)
20 kb Resolution Bin Reads (log10)
5 kb Resolution Bin Reads (log10)
B
Linkage Group VI
ΔK27 N4933 Hi-C DpnII, raw
ΔK27 N4933 Hi-C DpnII KR correct
C
Linkage Group VI
0 kb
100
200
300
400
500 kb
WT N150 DpnII Hi-C
ΔK27 N4933 DpnII Hi-C
5 kb Resolution Bin Reads (log10)
WT H3K27me2/3
WT H3K9me3
genes
D
E
LGVI L tel
LGVI R tel
LGV R tel
WT N150
ΔK27 N4933

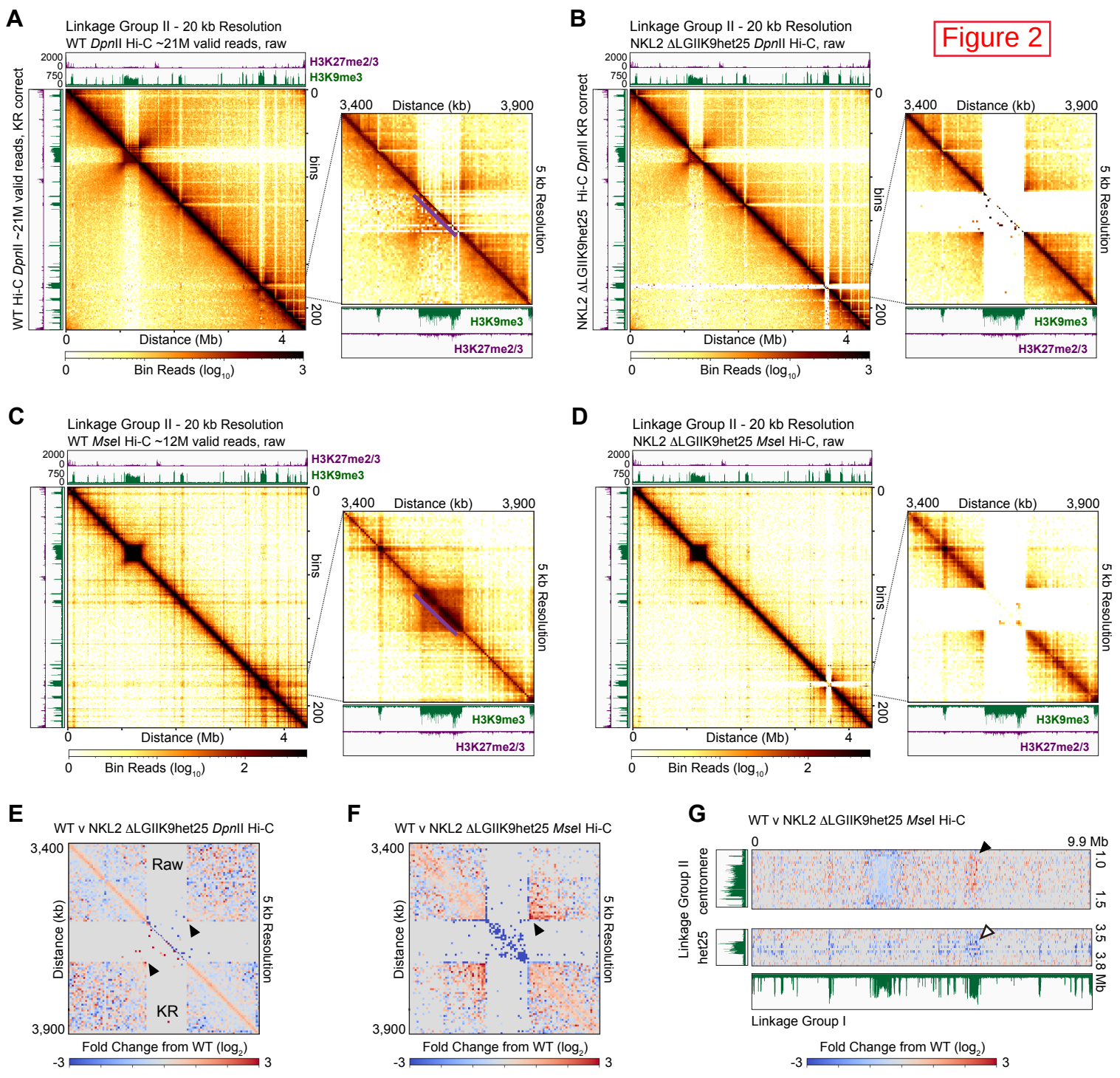
Figure 2
A
Linkage Group II - 20 kb Resolution
WT DpnII Hi-C ~21M valid reads, raw
H3K27me2/3
H3K9me3
WT Hi-C DpnII ~21M valid reads, KR correct
bins
Distance (Mb)
Bin Reads (log10)
3,400
Distance (kb)
3,900
5 kb Resolution
B
Linkage Group II - 20 kb Resolution
NKL2 ΔLGIIK9het25 DpnII Hi-C, raw
NKL2 ΔLGIIK9het25 Hi-C DpnII KR correct
C
Linkage Group II - 20 kb Resolution
WT MseI Hi-C ~12M valid reads, raw
D
Linkage Group II - 20 kb Resolution
NKL2 ΔLGIIK9het25 MseI Hi-C, raw
E
WT v NKL2 ΔLGIIK9het25 DpnII Hi-C
Raw
KR
Distance (kb)
Fold Change from WT (log2)
F
WT v NKL2 ΔLGIIK9het25 MseI Hi-C
G
WT v NKL2 ΔLGIIK9het25 MseI Hi-C
9.9 Mb
Linkage Group II
centromere
het25
Linkage Group I

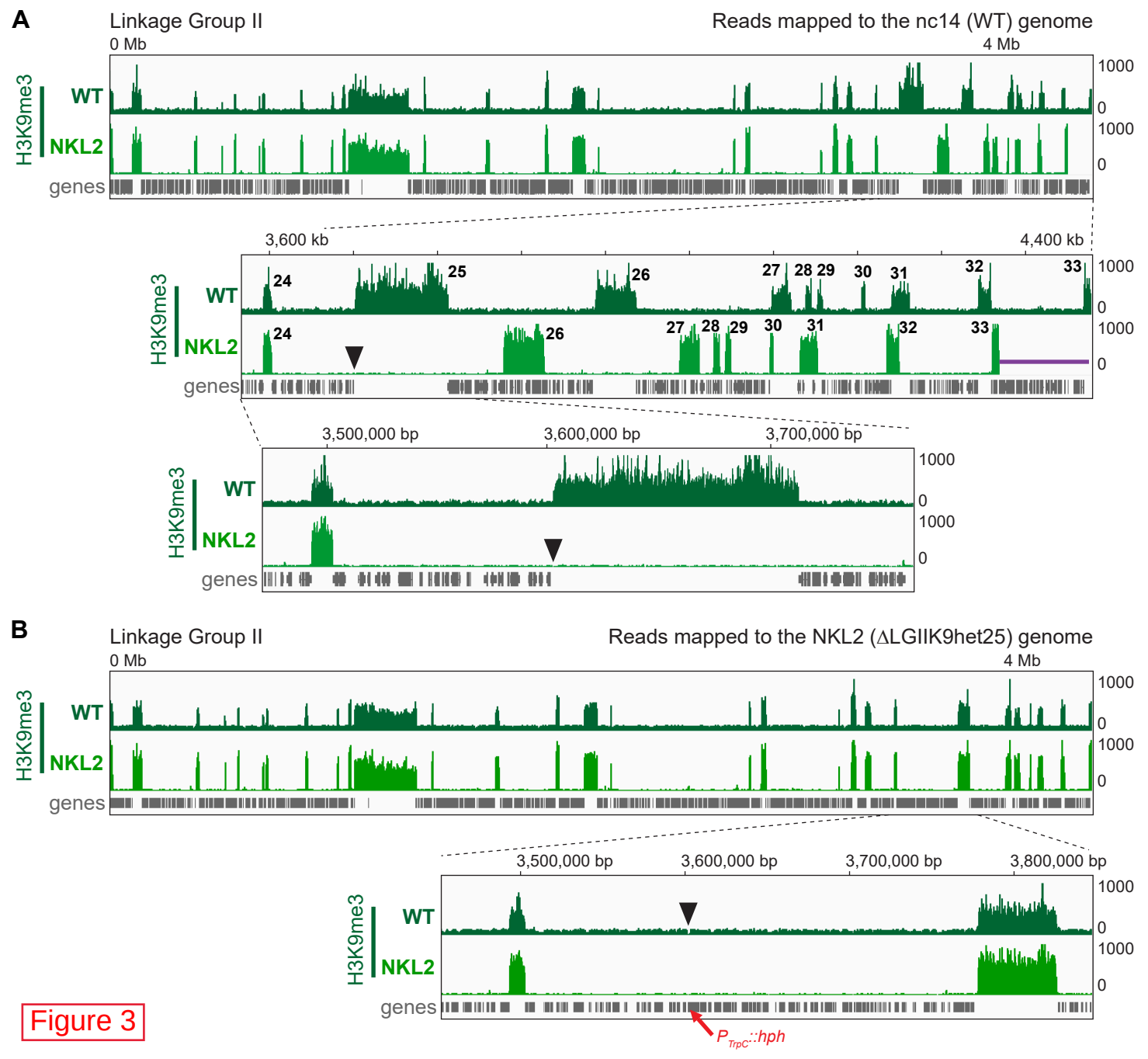
A
Linkage Group II
Reads mapped to the nc14 (WT) genome
0 Mb
4 Mb
H3K9me3
WT
NKL2
genes
1000
0
3,600 kb
4,400 kb
24
25
26
27
28
29
30
31
32
33
3,500,000 bp
3,600,000 bp
3,700,000 bp
B
Linkage Group II
Reads mapped to the NKL2 (ΔLGIIK9het25) genome
3,800,000 bp
P_{TrpC}::hph
Figure 3

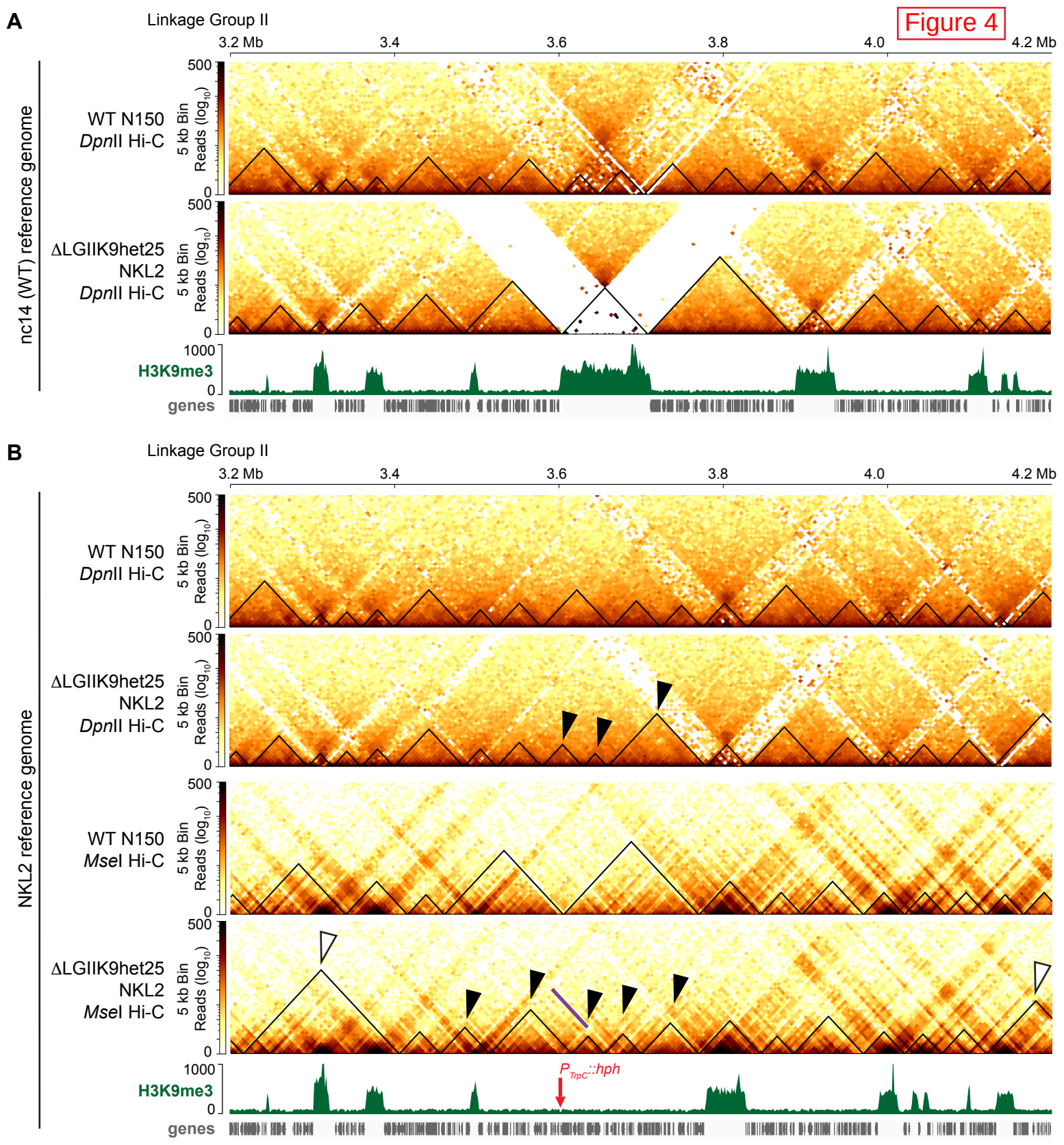
Figure 4
A
Linkage Group II
3.2 Mb
3.4
3.6
3.8
4.0
4.2 Mb
nc14 (WT) reference genome
WT N150
DpnII Hi-C
ΔLGIIK9het25
NKL2
DpnII Hi-C
5 kb Bin
Reads (log10)
500
0
1000
H3K9me3
genes
B
Linkage Group II
NKL2 reference genome
WT N150
DpnII Hi-C
ΔLGIIK9het25
NKL2
DpnII Hi-C
WT N150
MseI Hi-C
ΔLGIIK9het25
NKL2
MseI Hi-C
PTrpC::hph

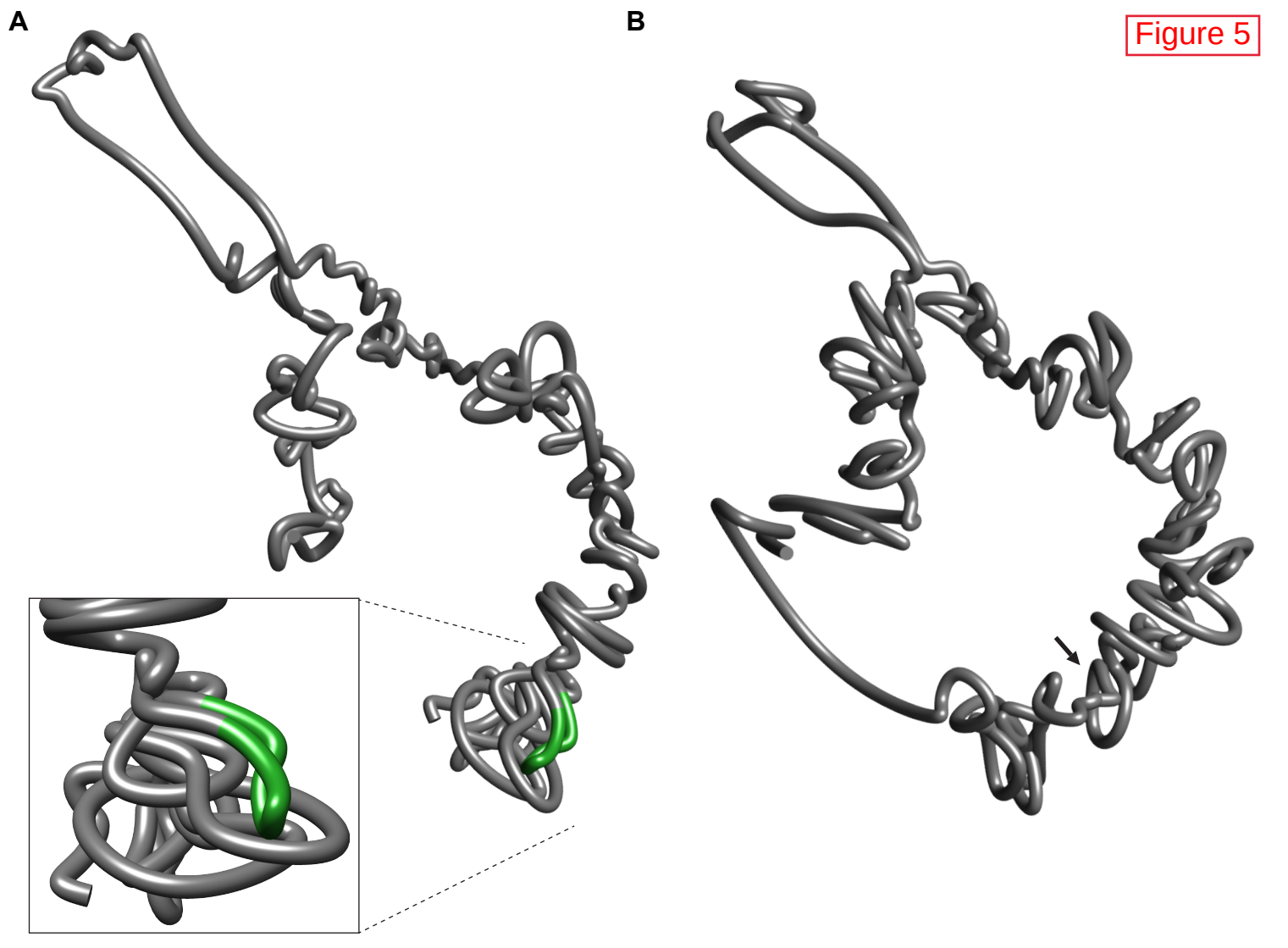
A
B
Figure 5

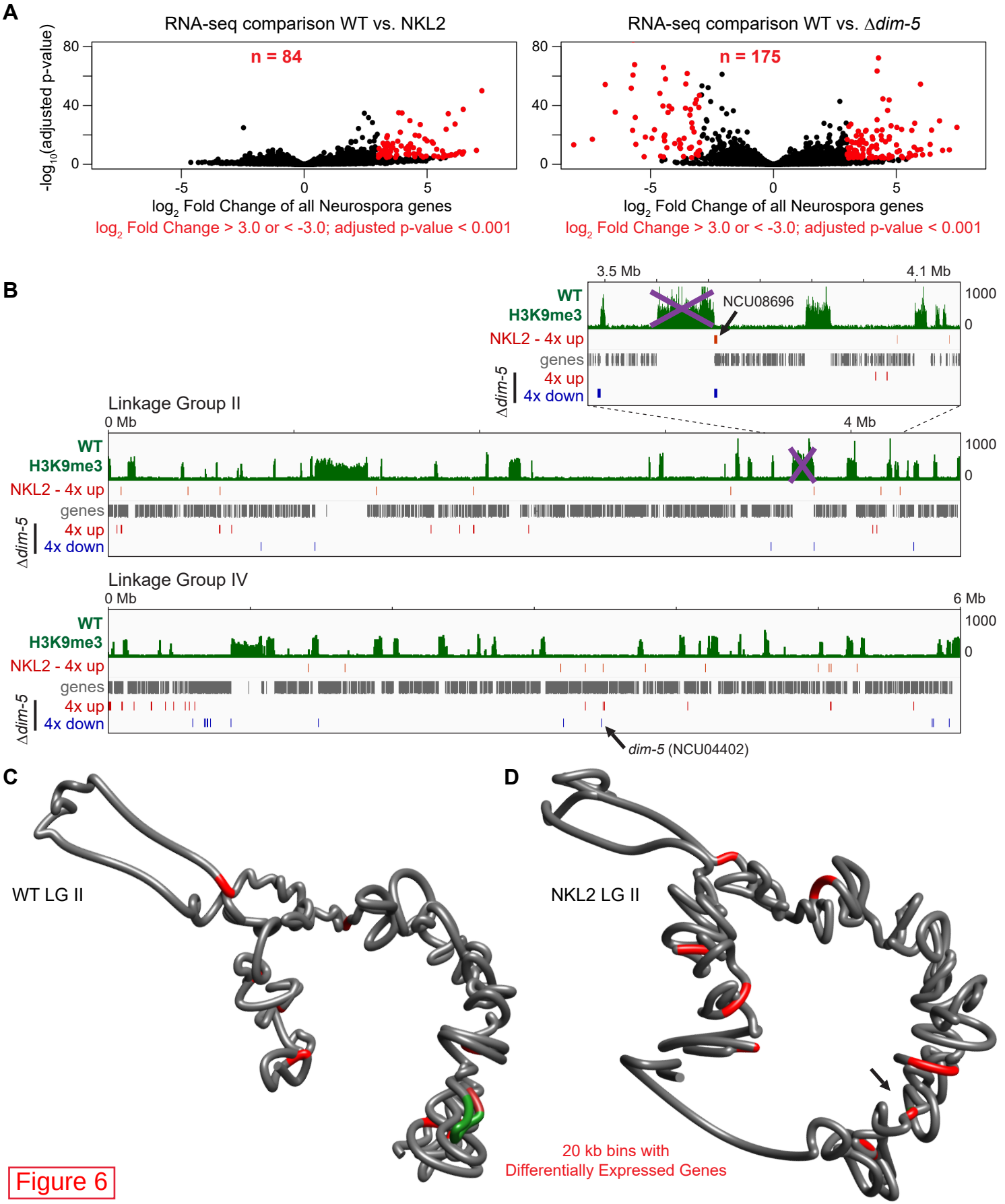
A
RNA-seq comparison WT vs. NKL2
n = 84
-log10(adjusted p-value)
log2 Fold Change of all Neurospora genes
log2 Fold Change > 3.0 or < -3.0; adjusted p-value < 0.001
RNA-seq comparison WT vs. Δdim-5
n = 175
log2 Fold Change of all Neurospora genes
log2 Fold Change > 3.0 or < -3.0; adjusted p-value < 0.001
B
3.5 Mb
4.1 Mb
WT
H3K9me3
NCU08696
NKL2 - 4x up
genes
Δdim-5
4x up
4x down
Linkage Group II
0 Mb
4 Mb
Linkage Group IV
6 Mb
dim-5 (NCU04402)
C
WT LG II
D
NKL2 LG II
20 kb bins with
Differentially Expressed Genes

Figure 6

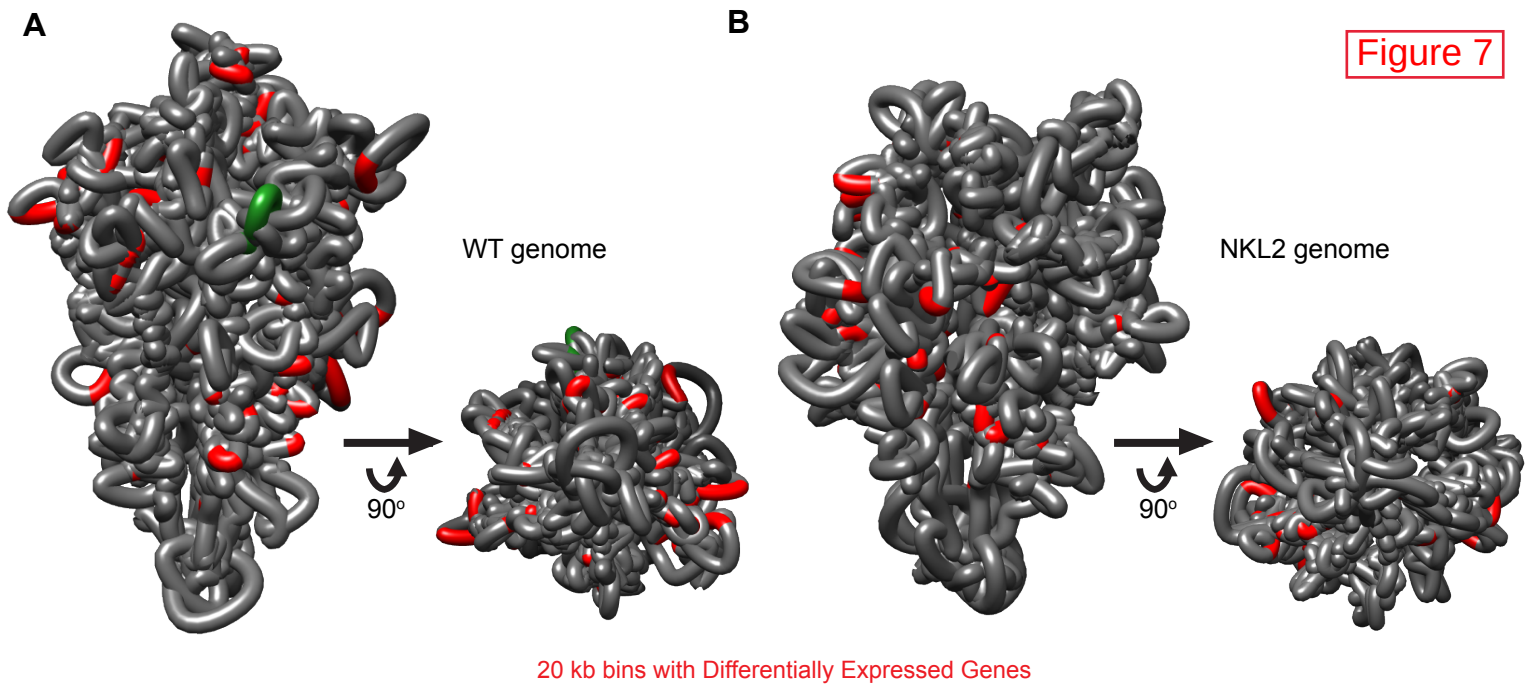
A
B
Figure 7
WT genome
NKL2 genome
90°
90°
20 kb bins with Differentially Expressed Genes